Two-network Kuramoto-Sakaguchi model under tempered stable Lévy noise

Alexander C. Kalloniatis,[1,*] Timothy A. McLennan-Smith,[2,†] Dale O. Roberts,[2,‡] and Mathew L. Zuparic[1,§]
[1]*Defence Science and Technology Group, Canberra, ACT 2600, Australia*
[2]*Australian National University, Canberra, ACT 2601, Australia*

(Received 9 August 2018; published 7 January 2019)

We examine a model of two interacting populations of phase oscillators labeled "blue" and "red." To this we apply tempered stable Lévy noise, a generalization of Gaussian noise where the heaviness of the tails parametrized by a power law exponent α can be controlled by a tempering parameter λ. This system models competitive dynamics, where each population seeks both internal phase synchronization and a phase advantage with respect to the other population, subject to exogenous stochastic shocks. We study the system from an analytic and numerical point of view to understand how the phase lag values and the shape of the noise distribution can lead to steady or noisy behavior. Comparing the analytic and numerical studies shows that the bulk behavior of the system can be effectively described by dynamics in the presence of tilted ratchet potentials. Generally, changes in α away from the Gaussian noise limit $1 < \alpha < 2$ disrupt the locking between blue and red, while increasing λ acts to restore it. However, we observe that with further decreases of α to small values $\alpha \ll 1$, with $\lambda \neq 0$, locking between blue and red may be restored. This is seen analytically in a restoration of metastability through the ratchet mechanism, and numerically in transitions between periodic and noisy regions in a fitness landscape using a measure of noise. This nonmonotonic transition back to an ordered regime is surprising for a linear variation of a parameter such as the power law exponent and provides a mechanism for guiding the collective behavior of such a complex competitive dynamical system.

DOI: 10.1103/PhysRevE.99.012205

I. INTRODUCTION

Many biological, social, and economic examples of complex systems contain both cooperative and competitive phenomena in tension that lead to both ordered and disordered behaviors. Various stylized features of these systems have been studied through the Kuramoto model [1] of synchronizing oscillators and its many extensions; see the review articles [2–6].

In this paper, we study synchronization in what we call the "blue vs red" model [7,8] under the effect of heavy-tailed stochastic perturbations. This model extends the Kuramoto-Sakaguchi oscillator model (e.g., see [4–6]) to the case of two interacting populations of oscillators attempting to synchronize with each other under various frustrations. More precisely, we consider N blue agents in an undirected network given by adjacency matrix $\mathscr{B}_{ij}$ $(i, j \in \{1, \ldots, N\} = \mathscr{B})$, and M red agents in an undirected network given by adjacency matrix $\mathscr{R}_{ij}$ $(i, j \in \{1, \ldots, M\} = \mathscr{R})$. Let $\beta_i \in \mathbf{R}$ denote the phase of the blue agent $i \in \mathscr{B}$ and $\rho_i \in \mathbf{R}$ the phase of the red agent $i \in \mathscr{R}$. The nonlinear dynamical system we consider is

$$\begin{aligned}\dot{\beta}_i &= \omega_i - \zeta_B \sum_{j\in\mathscr{B}} \mathscr{B}_{ij} \sin(\beta_i - \beta_j) \\ &\quad + f_{BR}(\beta_i, \rho) + \xi_i, \quad i \in \mathscr{B} \\ \dot{\rho}_i &= \nu_i - \zeta_R \sum_{j\in\mathscr{R}} \mathscr{R}_{ij} \sin(\rho_i - \rho_j) \\ &\quad + f_{RB}(\rho_i, \beta) + \tilde{\xi}_i, \quad i \in \mathscr{R}\end{aligned} \tag{1}$$

where $\xi_i, \tilde{\xi}_i$ are time-varying independent heavy-tailed white noises and f_{BR} and f_{RB} are interaction terms between the red and blue networks. These nonlinear interaction terms are given by

$$\begin{aligned}f_{BR}(\beta_i, \rho) &= -\zeta_{BR} \sum_{j\in\mathscr{R}} \mathscr{A}^{(BR)}_{ij} \sin(\beta_i - \rho_j - \phi), \\ f_{RB}(\rho_i, \beta) &= -\zeta_{RB} \sum_{j\in\mathscr{B}} \mathscr{A}^{(RB)}_{ij} \sin(\rho_i - \beta_j - \psi),\end{aligned} \tag{2}$$

where the matrices $\mathscr{A}^{(BR)}$ and $\mathscr{A}^{(RB)}$ of size $N \times M$ and $M \times N$, respectively, are adjacency matrices representing the undirected and unweighted edges from "blue to red" (BR) and "red to blue" (RB). We assume that $\mathscr{A}^{(BR)} = \mathscr{A}^{(RB)^T}$ so that the edges between blue and red populations are symmetric. These interaction terms contain temporal lags ϕ and ψ, often called frustrations, between the populations similar to the Sakaguchi variation [9–12] of the Kuramoto model. This typically drives a tendency to disorder in tension with the ordering tendency of synchronization.

Extending the Kuramoto model to multinetworks offers a viable approach to modeling competitive dynamics between ecological, social, and organizational populations [7,8,13–18], hence, our use of the labels red and blue. It has been shown that richer behavior in the dynamics of such models is observed under various forms of Gaussian white or colored

*alexander.kalloniatis@dst.defence.gov.au
†timothy.mclennan-smith@anu.edu.au
‡dale.roberts@anu.edu.au
§mathew.zuparic@dst.defence.gov.au

noise perturbations [3,19–26]. Recent studies have also shown relationships between the heaviness of the noise distribution's tails and synchronization behavior of the Kuramoto model [27,28]. The case of tempered stable noise, which we consider here, is particularly interesting due to its relation with tempered fractional diffusion [29–34] and is part of a broader class of processes called Lévy processes. At the core is the so-called stable Lévy noise where the stochastic process arises from a distribution with a heavy tail and scale law parametrized by an exponent α. As α is decreased from $\alpha = 2$, the noise deviates more strongly from Gaussian noise, and the tails become heavier with significant changes to the distribution below $\alpha = 1$. From a modeling perspective, *tempered* stable noise offers a number of useful attributes such as a small number of parameters, finite moments of all order, and a parameter λ that controls the tempering of the distribution's tails. Moreover, our approximations hold in a regime at the interface between order and noisy behavior, which is often where competing populations seek to operate.

A key question will be how the tempered stable noise changes dynamics observed for the deterministic [7] and Gaussian stochastic [8] versions of the blue-red system. As in these works, we explore the dynamics of our model from both an analytic and a numerical point of view. Indeed, in [7] we showed that much of the full dynamics of the system could be understood through linearization around a fixed point describing, respectively, internally synchronized blue and red clusters and examining the system in the vicinity of the regime where blue and red lose relative phase locking, and the role of a projection of the system into zero and normal modes of Laplacians of the networks. In the locked configuration, whichever of blue or red is ahead in phase by an amount less than π may be deemed to have a competitive advantage over the other. The system is thus poised at this interface between order and noisy behavior, with a transition through periodic behavior where blue and red remain internally synchronized but drifting in relation to each other. It turns out that this regime corresponds to a particle in a ratchet potential, which is a superposition of an oscillatory potential on a linear slope. In such systems, there is an interplay of the size of the wells and the slope determining if the particle may become trapped or rolls down the slope. In the blue-red system, this maps to the property that blue and red clusters lock, respectively drift, with respect to each other; drift would mean that blue and red rotate and thus the overall dynamics is periodic in time. In [8] we went on to show how this structure figured in the stochastic system, such that noise could trigger metastability, namely, situations where even though deterministically blue and red may be locked with respect to each other, noise would enable drift and thus periodic behavior. Nevertheless, this analysis showed that the deterministic fixed point system leaves its fingerprint on the stochastic dynamics. Nevertheless, as the type of noise becomes more exotic, the potential for disruption of global synchronization in the pure Kuramoto model, or locking for multiple populations, increases.

In this paper, we uncover a type of behavior that is not merely incremental to previous insights, namely, transitions between order, periodicity, and noisy behavior within the aforementioned nonlinear mechanism of metastability. Specifically, we discover a mechanism for restoring locking between blue and red in the presence of noise, or even diminishing the drift between the two when the system is deterministically periodic in behavior.

The key results of this paper are several: we may analytically derive transitions to and away from disruption of locking between blue and red for particular parameter ranges of the tempered stable Lévy noise in a regime where the deterministic system shows locked behavior (in Fig. 1); in numerical computation for the full nonlinear dynamics both individual paths (Figs. 2 and 3) of the fitness landscape for frustration parameters ϕ and ψ the imprint of the deterministic dynamics (Fig. 5) survives for weak noise strength across a range of values for the power and tempering indices of the tempered stable Lévy noise (Fig. 6); and this shows a transition from noisy behavior back to locking (Fig. 9) in the regime predicted in the analytic approach. What is genuinely surprising is that this restoration of locking or suppression of drift in the presence of tempered stable Lévy noise occurs for $\alpha \ll 1$ where naively the heavy tails of the stable noise case are extreme; in the absence of tempering, decreasing α only destroys locking with monotonically increasing severity (Fig. 8). Both the generalization of such a two-network frustrated Kuramoto model to tempered stable Lévy noise, and the detection of transitions to and from noisy behavior of a nonlinear model of multiple competing populations of synchronizing and frustrated oscillators is, to our understanding, different.

To this end, this paper is organized in the following manner. Section II provides the preliminary details of our setup, in particular, this part gives details about the network's interactions and how we model the heavy-tailed noise injected into the system. Section III provides an analytical approximation of the dynamics of the system near certain locked states for the deterministic version of the model and details the choice of networks used later in the numerical analysis. Section IV discusses analytical results for the stochastic model in some special cases. Here, we establish the result that the zero modes of the system are described by dynamics in the presence of tilted ratchet potentials manifesting metastability in regimes that would otherwise have been expected to be noisy. Section V focuses on the full nonlinear dynamics of the system using numerical simulations with aim to identify optimal internal synchronization and phase lag of the blue network against the red network. We achieve these results using Bayesian optimization to maximize an appropriately chosen objective function. We also study the presence of noisy paths given the choice of parameters in our noise through the implementation of the 0-1 test. Section VI provides a discussion on the extension of our numerical optimization to a wider parameter set.

II. PRELIMINARIES

In this section we give details on the various elements needed to specify and analyze the model in Eq. (1), detailing the network interactions between the blue and red networks, the implementation of the tempered stable Lévy noise, and the measure of sychronization within the two networks.

A. Network interactions and coupling

The $(N + M) \times (N + M)$ adjacency matrix for the corresponding external blue-red connections, labeled $\mathscr{M}$, has the

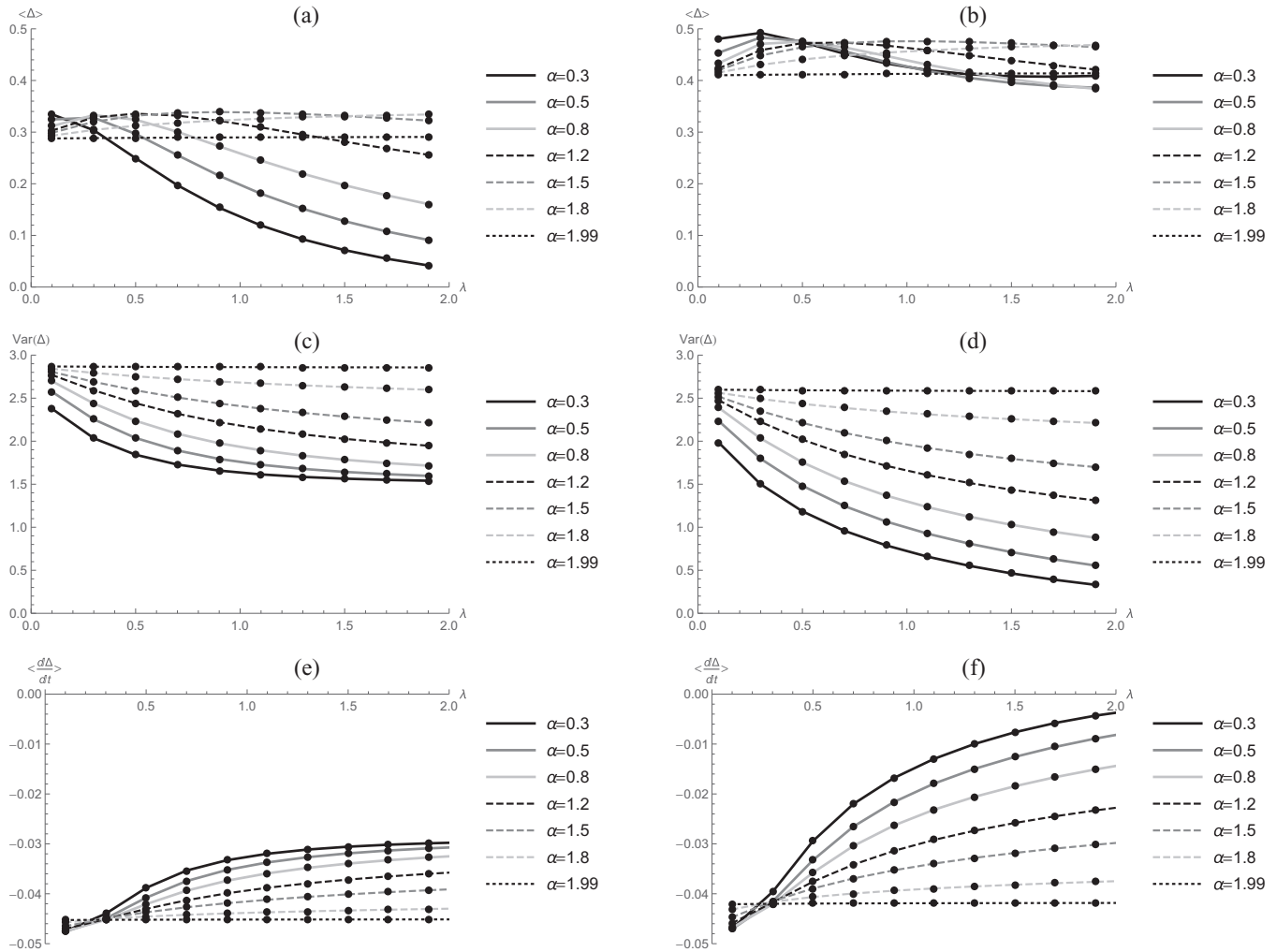

FIG. 1. Plots of the average [(a) and (b)] and variance [(c) and (d)] of Δ and the velocity $\langle\dot{\Delta}\rangle$ [(e) and (f)] given by Eq. (56) as a function of the tempering parameter λ for different values of the stability parameter α. The couplings are as in Eqs. (40) and the noise strength $\sigma = 0.1$. The left hand plots show when the frustration parameters are $\phi = 0.96\pi,\ \psi = 0$ (when blue and red deterministically drift) and the right hand the case for $\phi = 0.94\pi,\ \psi = 0$ (where blue and red deterministically lock).

following block off-diagonal form:

$$\mathscr{M} = \begin{pmatrix} 0 & \mathscr{A}^{(BR)} \\ \mathscr{A}^{(RB)} & 0 \end{pmatrix}.$$

The quantities ω_i, ν_i in Eq. (1) give the natural frequencies of the associated blue and red agents, respectively; they may be drawn from some probability distribution. Finally, ζ_B, ζ_R, ζ_{BR}, ζ_{RB} in Eqs. (1) and (2) are coupling constants, respectively, for intra-blue, intra-red, blue to red, and red to blue interactions. Asymmetry between blue and red potentially exists in the coupling constants and frustrations. That is, ζ_{BR} and ζ_{RB}, and ϕ and ψ need not be equal.

B. Tempered stable Lévy noise

The stochastic terms in our system can be rewritten by considering a stochastic differential equation formulation of our system by formally multiplying both sides of Eq. (1) by dt and assume $\xi_i\, dt = dL_i(t)$ where $L_i = (L_i(t))_{t\geqslant 0}$ is a Lévy process for $i = 1, \ldots, N$; see [35] for a general introduction to Lévy processes. We do the same for the $\tilde{\xi}_i$ for $i = 1, \ldots, M$ terms which are simply independent copies. This gives us $N + M$ noise terms that we relabel L_i for $i = 1, \ldots, N + M$. We now assume that these processes are tempered stable Lévy processes which is a subclass that has three parameters governing the distribution of their increments: the stability parameter α, the tempering parameter λ, and the asymmetry parameter θ. From the Lévy-Khintchine formula, the characteristic exponent Λ satisfying $\mathbb{E}[e^{kL_i(t)}] = e^{t k\Lambda(k)}$ of the process is given by $\Lambda(k) := C(k)$ for $0 < \alpha < 1$ and $\Lambda(k) := C(k) - 2ik\alpha\theta\lambda^{\alpha-1}$ for $1 < \alpha < 2$ where

$$C(k) := -\frac{1}{2\cos(\alpha\pi/2)}[(1+\theta)(\lambda + ik)^\alpha + (1-\theta)(\lambda - ik)^\alpha - 2\lambda^\alpha]. \tag{3}$$

The probability density $p(x, t)$ of each process L_i for $i = 1, \ldots, N + M$ satisfies a tempered fractional diffusion equation $x = L_i(t)$,

$$\partial_t p(x, t) = c\partial_x^{\alpha,\theta,\lambda} p(x, t), \tag{4}$$

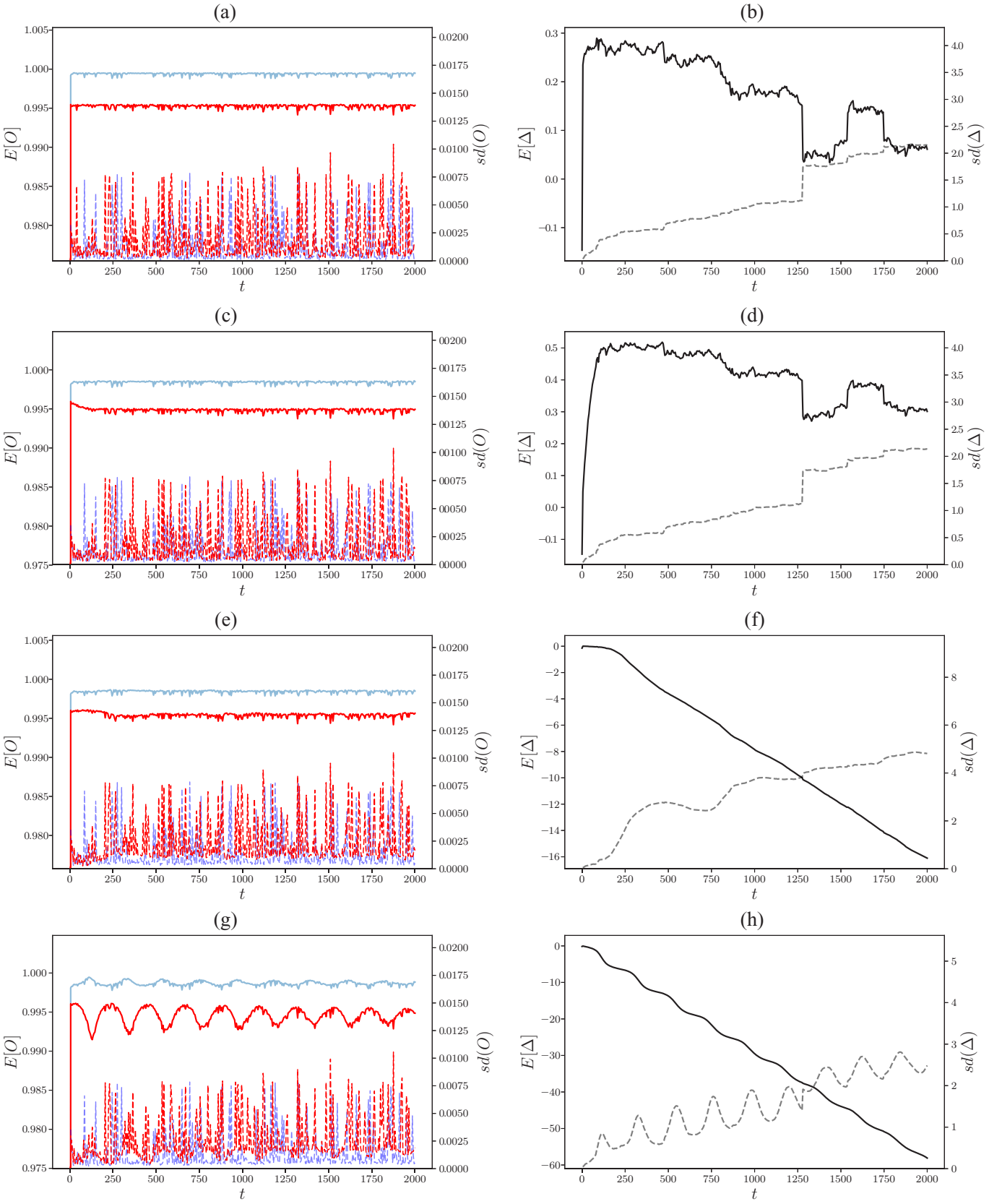

FIG. 2. Time series plots in the stable Lévy noise case with $\sigma = 0.05$ and $\alpha = 1.5$. Left axis: time series plots for the average order parameters and Δ. Right axis: time series plots (dashed lines) for the standard deviation of the Monte Carlo estimates of the order parameters and Δ. Left column: order parameters for the blue and red networks as given by the blue (light gray) and red (gray) lines, respectively. Right column: Δ as denoted by the black lines. (a), (b) $(\phi, \psi) = (0.2\pi, 0)$; (c), (d) $(\phi, \psi) = (0.94\pi, 0)$; (e), (f) $(\phi, \psi) = (0.95\pi, 0)$; (g), (h) $(\phi, \psi) = (0.96\pi, 0)$.

where the constant $c > 0$ for $1 < \alpha < 2$ and $c < 0$ for $0 < \alpha < 1$ and the tempered-fractional-diffusion operator $\partial_x^{\alpha,\theta,\lambda}$ is given explicitly as [33,34]

$$\partial_x^{\alpha,\theta,\lambda} = \mathscr{D}_x^{\alpha,\theta,\lambda} + v^{\alpha,\theta,\lambda}\frac{\partial}{\partial x} + \nu^{\alpha,\lambda}, \tag{5}$$

where $v^{\alpha,\theta,\lambda}$ and $\nu^{\alpha,\lambda}$ are additional drift and source (sink) terms given by

$$v^{\alpha,\theta,\lambda} = \begin{cases} 0, & \alpha \in (0,1) \\ \frac{\alpha\theta\lambda^{\alpha-1}}{|\cos(\pi\alpha/2)|}, & \alpha \in (1,2) \end{cases}, \quad \nu^{\alpha,\lambda} = \frac{\lambda^\alpha}{\cos(\pi\alpha/2)}. \tag{6}$$

Here, $\alpha \in (0,1) \cup (1,2]$ is the fractional power or stability parameter, governing the heavy-tail law of the distribution generating the noise, $\theta \in [-1,1]$ is an asymmetry generating skew in the distribution, and $\lambda \in (0,\infty)$ is a tempering parameter that exponentially suppresses large jumps in the process η. Importantly, we take the noise as *centered* in the Gaussian limit (zero mean). For stability parameter $\alpha = 2$, the Lévy noise becomes Gaussian and the tempering λ no longer has any effect. Importantly, the value $\alpha = 1$ is excluded because it corresponds to the pathological Cauchy process. The operator $\mathscr{D}_x^{\alpha,\theta,\lambda}$ is called the λ-truncated fractional derivative of order α, given by

$$\mathscr{D}_x^{\alpha,\theta,\lambda} = l(\theta)e^{-\lambda x}\,{}_{-\infty}D_x^\alpha e^{\lambda x} - r(\theta)e^{\lambda x}\,{}_xD_\infty^\alpha e^{-\lambda x}, \tag{7}$$

where the operators ${}_{-\infty}D_x^\alpha$ and ${}_xD_\infty^\alpha$ are the Riemann-Liouville derivatives defined as [34]

$$e^{-\lambda x}\,{}_{-\infty}D_x^\alpha e^{\lambda x} f(x) = \frac{e^{-\lambda x}}{\Gamma(m-\alpha)}\frac{\partial^m}{\partial x^m} \times \int_{-\infty}^x \frac{d\zeta e^{\lambda\zeta}}{(x-\zeta)^{\alpha+1-m}} f(\zeta), \tag{8}$$

$$e^{\lambda x}\,{}_xD_\infty^\alpha e^{-\lambda x} f(x) = \frac{(-1)^m e^{\lambda x}}{\Gamma(m-\alpha)}\frac{\partial^m}{\partial x^m} \times \int_x^\infty \frac{d\zeta e^{-\lambda\zeta}}{(\zeta-x)^{\alpha+1-m}} f(\zeta) \tag{9}$$

for $\alpha - 1 < m < \alpha$. These can be equivalently defined in Fourier space [36,37]

$$\begin{aligned} \mathscr{F}\left[e^{-\lambda x}\,{}_{-\infty}D_x^\alpha e^{\lambda x} f(x)\right] &= (\lambda - ik)^\alpha \hat{f}(k), \\ \mathscr{F}\left[e^{\lambda x}\,{}_xD_\infty^\alpha e^{-\lambda x} f(x)\right] &= (\lambda + ik)^\alpha \hat{f}(k), \end{aligned} \tag{10}$$

where

$$\begin{aligned} \mathscr{F}[f(x)] &= \int_{-\infty}^\infty dx\, e^{ikx} f(x) = \hat{f}(k), \\ \mathscr{F}^{-1}[\hat{f}(k)] &= \int_{-\infty}^\infty \frac{dk}{2\pi} e^{-ikx}\hat{f}(k) = f(x). \end{aligned} \tag{11}$$

The weighting factors

$$l(\theta) = \frac{\theta - 1}{2\cos(\pi\alpha/2)}, \quad r(\theta) = \frac{\theta + 1}{2\cos(\pi\alpha/2)} \tag{12}$$

determine the asymmetry imposed on each of the Riemann-Liouville derivatives. It is also useful to take the Fourier transform of the fractional derivative $\partial_x^{\alpha,\theta,\lambda}$ giving

$$\mathscr{F}\left[\partial_x^{\alpha,\theta,\lambda} f(x)\right] = \underbrace{\{l(\theta)(\lambda - ik)^\alpha - r(\theta)(\lambda + ik)^\alpha - ikv^{\alpha,\theta,\lambda} + \nu^{\alpha,\lambda}\}}_{=\Lambda(k)/\sigma^2}\widehat{f}(k), \tag{13}$$

where $\Lambda(k)$ is the characteristic exponent (given earlier) and σ^2 becomes the variance of the noise in the Gaussian limit. The centered noise is specified by four parameters $\alpha, \sigma, \theta, \lambda$, generalizing from the one parameter of mean-zero Gaussian noise σ that we obtain in the limit as $\alpha \to 2$.

C. Measures of synchronization

To measure the degree of synchronization within a given population we use local forms of Kuramoto's order parameter [1] given by

$$O_B = \frac{1}{N}\left|\sum_{j\in\mathscr{B}} e^{i\beta_j}\right|, \quad O_R = \frac{1}{M}\left|\sum_{j\in\mathscr{R}} e^{i\rho_j}\right|.$$

We emphasize that in many of our examples in the following the total system ("global") order parameter $1/(N+M)|\sum_{i\in\mathscr{B}} e^{i\beta_i} + \sum_{j\in\mathscr{R}} e^{i\rho_j}|$ will be far from the value one.

III. BULK DYNAMICS NEAR LOCKED STATES

In this section we make various approximations to understand the bulk dynamics analytically when the system is near certain locked states. In Sec. V we return to the studying the full system (without approximations), albeit numerically.

There are various ways that the system can be deemed locked. We refer to the phase locking within blue, that is $\beta_i \approx \beta_j\ \forall\ i, j \in \mathscr{B}$, and within red $\rho_i \approx \rho_j\ \forall\ i, j \in \mathscr{R}$, as *internal* or *local locking*, and the phase locking of blue externally with red, $\beta_i \approx \rho_j\ \forall\ \{i, j\} \in \{\mathscr{B}, \mathscr{R}\}$, as *external* or *global phase locking*. If we denote by B and P the centroids of the blue and red phases given by

$$B = \frac{1}{N}\sum_{i\in\mathscr{B}} \beta_i, \quad P = \frac{1}{M}\sum_{i\in\mathscr{R}} \rho_i, \tag{14}$$

and consider the difference

$$\Delta(t) \equiv B(t) - P(t), \tag{15}$$

then if $\Delta \neq 0$ is time independent then we may speak of external *frequency locking*.

A. Two-cluster ansatz

In general, the system in Eq. (1) can only be solved numerically. To gain analytic insight in a region of greatest relevance, given that blue and red may deem internal phase synchronization ideal, we explore a fixed point given by the ansatz

$$\beta_i(t) = B(t) + b_i(t), \quad \rho_j = P(t) + p_j(t), \quad \forall\ \{i, j\} \in \{\mathscr{B}, \mathscr{R}\}, \tag{16}$$

with b_i, p_j small so that $b_i^2 \approx 0$, $p_j^2 \approx 0$. This leads to $\sum_{i\in\mathscr{B}} b_i = \sum_{i\in\mathscr{R}} p_i = 0$. To correctly take into account the noise terms, we rewrite our system in the stochastic differential equation formulation by formally multiplying both sides of Eq. (1) by dt and assume $\xi_i\, dt = dL_i(t)$ where $L_i(t)$ is a tempered stable Lévy process as introduced in Sec. II B. We then linearize the system given by Eq. (1), keeping only terms first order in a Taylor expansion, then using the ansatz given by Eqs. (16) and (15) we obtain the linearized dynamics

$$db_i(t) = \Big[-B(t) + \Omega_i(t) - \zeta_B \sum_{j\in\mathscr{B}} \mathscr{L}_{ij}^{(B)} b_j(t) - \zeta_{BR}\cos[\Delta(t)-\phi] \sum_{j\in\mathscr{B}\cup\mathscr{R}} \mathscr{L}_{ij}^{(BR)} v_j \Big] dt + dL_i(t),$$
$$dp_i(t) = \Big[-P(t) + \Omega_i(t) - \zeta_R \sum_{j\in\mathscr{R}} \mathscr{L}_{ij}^{(R)} p_j - \zeta_{RB}\cos[\Delta(t)+\psi] \sum_{j\in\mathscr{B}\cup\mathscr{R}} \mathscr{L}_{ij}^{(RB)} v_j \Big] dt + dL_i(t), \tag{17}$$

where

$$v_i = \begin{cases} b_i, & i\in\mathscr{B} \\ p_i, & i\in\mathscr{R} \end{cases}, \quad \Omega_i(t) = \begin{cases} \omega_i - \zeta_{BR}\, d_i^{(BR)} \sin[\Delta(t)-\phi], \\ \nu_i + \zeta_{RB}\, d_i^{(RB)} \sin[\Delta(t)+\psi]. \end{cases}$$

The quantities d and $\mathscr{L}$, with superscripts B, R, BR, and RB, represent, respectively, the degree and corresponding Laplacian for the blue, red, blue-red, and red-blue networks using the matrix $\mathscr{M}$; see Appendix A. Note that the Laplacian is defined as $\mathscr{L} := D - A$ where D is the degree matrix and A is the adjacency matrix of the respective networks; see [13,38,39] for the significance of the Laplacian spectrum.

B. Decoupling and projecting the dynamics

In order to proceed analytically, we assume that

$$\sum_{j\in\mathscr{B}\cup\mathscr{R}} \mathscr{L}_{ij}^{(BR)} v_j \approx \sum_{j\in\mathscr{B}\cup\mathscr{R}} \mathscr{L}_{ij}^{(RB)} v_j \approx 0, \tag{18}$$

so that the equations for the fluctuations b_i and p_j in Eq. (17) may be decoupled through the use of the two intrapopulation Laplacians $\mathscr{L}^{(B)}$ and $\mathscr{L}^{(R)}$. As mentioned in [7,8], this approximation is not guaranteed to completely hold, either deterministically or under the influence of noise, in model regimes which enable Eq. (16) to be satisfied; we apply it to generate qualitative analytic expressions to enable understanding of macroscopic model behaviors. Nevertheless, for regimes of weak noise, it is seen to hold sufficiently that such insights are valid [7,8].

We factorize the Laplacian $\mathscr{L}^{(B)}$ using an eigendecomposition and order the eigenvalues as $0 = \lambda_0^{(B)} \leqslant \lambda_1^{(B)} \leqslant \cdots \leqslant \lambda_N^{(B)}$. Each eigenvalue has an associated eigenvector forming a complete spanning set of orthonormal eigenvectors for the N-dimensional subspaces that we label as $e^{(B,r)}$ for $r = 0, 1, \ldots, N-1 \in \mathscr{B}_E$. We perform the same procedure for $\mathscr{L}^{(R)}$, giving eigenvectors $e^{(R,r)}$ for $r = 0, 1, \ldots, M-1 \in \mathscr{R}_E$ with associated eigenvalues $\lambda_r^{(R)}$. We distinguish between indices in node space $\{\mathscr{B}, \mathscr{R}\}$ and those in eigenmode space $\{\mathscr{B}^E, \mathscr{R}^E\}$ (which has the same dimensionality) by reserving labels $\{i, j\}$ for expressions involving graph nodes, and labels $\{r, s\}$ for expressions involving Laplacian eigenmodes. We assume that blue and red networks each consist of one component. Up to normalization, the corresponding zero eigenvectors $\vec{e}^{(B,0)}$ and $\vec{e}^{(R,0)}$ consist of all unit valued entries [38].

We now successively project the dynamics in Eq. (17) onto the increasing eigenmodes $r = 0, 1, \ldots, N-1 \in \mathscr{B}_E$ and $r = 0, 1, \ldots, M-1 \in \mathscr{R}_E$. Combined with Eq. (14), we see that B and P are the zero-mode projections of the phases β_i and ρ_j. Analogously, we denote by x_r and y_s the projections of b_i and p_i on the blue and red nonzero eigenvectors. We give explicit expressions in Appendix A.

First we assume that the noise is zero to understand the core dynamics of the system. Using Eq. (18) and the eigenvector projections in Eq. (17) combined with the orthonormality of the eigenvectors gives

$$\dot{x}_r = \omega^{(r)} - \zeta_B \lambda_r^{(B)} x_r - \zeta_{BR} d_r^{(BR)} \sin(\Delta - \phi), \tag{19}$$

$$\dot{y}_s = \nu^{(s)} - \zeta_R \lambda_s^{(R)} y_s + \zeta_{RB} d_s^{(RB)} \sin(\Delta + \psi), \tag{20}$$

$$\dot{B} = \bar{\omega} - \frac{\zeta_{BR} d_T^{(BR)}}{N} \sin(\Delta - \phi), \tag{21}$$

$$\dot{P} = \bar{\nu} + \frac{\zeta_{RB} d_T^{(BR)}}{M} \sin(\Delta + \psi) \tag{22}$$

for $r \in \mathscr{B}^E/\{0\}$ and $s \in \mathscr{R}^E/\{0\}$. The terms $\omega^{(r)}$ and $d_r^{(BR)}$ are the projections onto the rth eigenvector and $\bar{\omega}$ is the average over $\mathscr{B}$ with $d_s^{(RB)}$ the projections onto the sth eigenvector and $\bar{\nu}$ the average frequency for red. The difference of $\dot{B}$ and $\dot{P}$ gives then

$$\dot{\Delta} = -V'(\Delta), \tag{23}$$

where

$$V(\Delta) = -\mu\Delta - \sqrt{S^2 + C^2}\cos(\Delta - \varrho), \tag{24}$$

$$\mu = (\bar{\omega} - \bar{\nu}), \tag{25}$$

$$\varrho \equiv \tan^{-1}(S/C), \tag{26}$$

$$C \equiv d_T^{(BR)} \left(\frac{\zeta_{BR}\cos\phi}{N} + \frac{\zeta_{RB}\cos\psi}{M} \right), \tag{27}$$

$$S \equiv d_T^{(BR)} \left(\frac{\zeta_{BR}\sin\phi}{N} - \frac{\zeta_{RB}\sin\psi}{M} \right). \tag{28}$$

Thus, Δ may be solved first from Eq. (23), and then used in the forcing terms of the normal mode equations in Eqs. (19) which are otherwise solvable in their own right.

The substitution $\Delta = \rho + 2\tan^{-1}(\vartheta + \frac{\sqrt{S^2+C^2}}{\mu})$ leads to the solution

$$\Delta(t) = \rho + 2\tan^{-1} \times \left\{ \sqrt{\frac{S^2+C^2}{\mu^2}} + \sqrt{\frac{\mathscr{K}}{\mu^2}} \tanh\left(\frac{\mathrm{sgn}(\mu)\sqrt{\mathscr{K}}}{2} (\mathrm{const} - t) \right) \right\}, \tag{29}$$

where $\mathrm{const} = \frac{2}{\sqrt{\mathscr{K}}} \tanh^{-1}\{\frac{\mu}{\sqrt{\mathscr{K}}}\vartheta_0\}$ and

$$\mathscr{K} = C^2 + S^2 - \mu^2. \tag{30}$$

The solutions to the normal modes are given in Appendix A. Ultimately, their dynamics depends on the behavior of $\Delta(t)$ which in turn is governed by the potential $V(\Delta)$ in Eq. (23). This is commonly referred to as a tilted periodic [40–42] or tilted Smoluchowski-Feynman ratchet [43] potential. Importantly, we have periodicity $V'(\Delta) = V'(\Delta + 2\pi)$, and the tilt refers to the constant forcing term in $V'(\Delta)$ given by the difference of frequency averages μ. The sign of $\mathscr{K}$ is critical. If $\mathscr{K} > 0$, the solution asymptotes to the value $\rho + \sin^{-1}(\frac{\mu}{\sqrt{S^2+C^2}})$ mod 2π. If $\mathscr{K} < 0$, then Eq. (29) gives oscillatory behavior with period $\frac{2\pi}{\sqrt{|\mathscr{K}|}}$. Alternately, for $\mathscr{K} > 0$, $V(\Delta)$ is a series of local maxima with unstable fixed points at $\Delta = \pi + \rho - \sin^{-1}(\frac{\mu}{\sqrt{S^2+C^2}}) + 2\pi n$, $n \in \mathbb{Z}$, and local minima with stable fixed points at $\Delta = \rho + \sin^{-1}(\frac{\mu}{\sqrt{S^2+C^2}}) + 2\pi n$, $n \in \mathbb{Z}$, on a landscape which has an overall slope according to the sign of μ. For $\mathscr{K} = 0$, the hills and valleys of the potential become points of inflection, and hence unstable fixed points. For $\mathscr{K} < 0$, the potential loses all of its fixed points, even the unstable ones. We may also speak of *drift* when there is no stable fixed point. This implies that blue and red clusters will be in motion with respect to each other.

C. Projecting the noise

We now consider how the noise gets projected onto the eigenmodes of the Laplacians. At every time point t, the increments of the processes $L_i^{(B)}(t)$ and $L_i^{(R)}(t)$ may be decomposed in terms of eigenvectors of the blue and red Laplacians as

$$\begin{aligned} dL_i^{(B)}(t) &= \sum_{r\in\mathscr{B}_E} \gamma_r^{(B)} e_i^{(B,r)} d\eta_r^{(B)}(t), \quad i \in \mathscr{B} \\ dL_i^{(R)}(t) &= \sum_{r\in\mathscr{R}_E} \gamma_r^{(R)} e_i^{(R,r)} d\eta_r^{(R)}(t), \quad i \in \mathscr{R} \end{aligned} \tag{31}$$

where $\eta_r^{(B)}$ and $\eta_r^{(R)}$ are also tempered stable Lévy processes but with different parameter values. This follows from the fact that projections of Lévy processes are also Lévy processes; see Proposition 11.10 in [35].

In [28] we derived the general expression for projection onto an N-dimensional vector u_j of the tempered stable Lévy process η_i:

$$dL_{\mathrm{proj}} = \sum_{j=1}^{N} u_j d\eta_j. \tag{32}$$

For the noise η this is defined as a function of the parameters $\alpha, \sigma, \theta, \lambda$, as in Eq. (13). Then, for the projected process L_{proj} the characteristic exponent is

$$\Lambda_{\mathrm{proj}}(k) = \sigma^2 \sum_{j=1}^{N} [(1+\theta)(\lambda + iku_j)^\alpha + (1-\theta)(\lambda - iku_j)^\alpha - iku_j v^{\alpha,\theta,\lambda} + \nu^{\alpha,\lambda}]. \tag{33}$$

Essentially, the "momentum" k is multiplied by the component of the vector u_j.

The system given in Eq. (19) with the noise reintroduced is a Langevin (i.e., Ornstein-Uhlenbeck) system, written in stochastic differential equation (SDE) form as

$$dx_r(t) = q_r^{(B)}(x_r(t), \Delta)dt + \gamma_r^{(B)} d\eta_r^{(B)}(t), \tag{34}$$

$$dy_s(t) = q_s^{(R)}(y_s(t), \Delta)dt + \gamma_s^{(R)} d\eta_s^{(R)}(t), \tag{35}$$

$$d\Delta(t) = -V'(\Delta)dt + \gamma_0^{(B)} d\eta_0^{(B)}(t) - \gamma_0^{(R)} d\eta_0^{(R)}(t) \tag{36}$$

for $r \in \mathscr{B}^E/\{0\}$, $s \in \mathscr{R}^E/\{0\}$, and where the variables and parameters are as used in Eq. (19).

D. Measures of synchronization and the fixed point approximation

Something absent in our previous work [7,8] is the centroid representation for order parameters

$$O_B = \frac{1}{N}\sqrt{\sum_{i,j\in\mathscr{B}} \cos^2(\beta_i - \beta_j)} = \frac{1}{N}\sqrt{\sum_{i,j\in\mathscr{B}} \cos^2(b_i - b_j)}, \tag{37}$$

$$O_R = \frac{1}{N}\sqrt{\sum_{i,j\in\mathscr{R}} \cos^2(\rho_i - \rho_j)} = \frac{1}{N}\sqrt{\sum_{i,j\in\mathscr{R}} \cos^2(p_i - p_j)}. \tag{38}$$

In the fixed point approximation when $\mathscr{K} > 0$ (giving Δ constant), b_i, p_i may be determined from the stationary solutions for x_r, y_r in Eqs. (19) which may be substituted into Eqs. (37) and (38). Alternatively, and reintroducing the $\mathscr{L}^{BR}$, $\mathscr{L}^{RB}$ matrices, Eq. (17) in the static limit may also be compactly written in terms of a "super-Laplacian" matrix $\mathscr{L}$,

$$\vec{\Omega} - \mathscr{L}\vec{v} = 0, \tag{39}$$

where the off-diagonal parts of the matrix $\mathscr{L}$ incorporate the terms ignored thus far [Eq. (18)]. The super-Laplacian, given explicitly in [7], is not symmetric but has zero column sum and therefore a single zero right eigenvalue. Thus, Eq. (39) is invertible through the pseudoinverse of the super-Laplacian (even though it may only be computed numerically, in general) and used in Eqs. (37) and (38).

Importantly, this brings together information about the network structure through the Laplacian, but also on the nature

of the threshold in $\mathscr{K}$ through the implicit dependence on Δ. Thus, any deterministic optimization of O_B (for example) in relation to parameters ϕ and ψ will encode the transition to periodic behavior at $\mathscr{K} = 0$. We will show a numerical example of this below when we consider the fitness landscape of the deterministic system.

E. Example networks, frequencies, and couplings

To illustrate our otherwise general solutions and compare to numerical simulation we consider an example of blue agents in a hierarchy and red agents on a random network. As in [7,8], for $\mathscr{B}$ we consider a complete k-ary tree, with $k = 4$, thus, $N = 21$. For $\mathscr{R}$ we use a random Erdös-Rényi network also of $N = 21$ with link of probability 0.4. The two networks, and further details of their interconnection, are shown in Appendix C in Fig. 10.

The specific frequencies of each agent are drawn from a uniform distribution $\omega_i, \nu_j \in [0, 1]$ and are plotted in Appendix C. In this instance, the average frequencies are $\bar{\omega} = 0.503$, $\bar{\nu} = 0.551$, giving $\mu = -0.048$. If cross couplings were set to zero, the red population would lap blue over time. The sign of μ here implies a negative slope for the tilted ratchet potential $V(\Delta)$.

We choose coupling values

$$\zeta_B = 8, \quad \zeta_R = 0.5, \quad \zeta_{BR} = \zeta_{RB} = 0.4. \tag{40}$$

These values give high internal phase synchronization [7,8]. Note that $\zeta_B > \zeta_R$, reflecting the difficulty of hierarchies to synchronize. In this respect, we have selected values that put quite different network structures on an approximately equal footing. Nevertheless, we derive results for the general network case. These couplings do allow for some changes in dynamics as the frustrations are varied; specifically, we set $\psi = 0$ and manipulate ϕ. Then, $\mathscr{K}$ changes sign from positive to negative at $\phi_c = 0.9498\pi$. In the vicinity of this point, in the absence of noise, for $\phi < \phi_c$ blue locks to a fixed phase ahead of red, and for $\phi \geqslant \phi_c$ blue and red remain internally phase synchronized but lap each other with a period that decreases as ϕ gets larger. Thus, we shall be interested in behaviors slightly below and above this point, for example, $\phi = 0.94\pi$ and 0.96π.

IV. ANALYTICAL RESULTS

In this section, we derive some analytic results when the system is perturbed by exogenous stochastic shocks. We seek to understand the bulk behavior through a projection onto an expansion in terms of the red and blue Laplacians.

A. Noisy normal modes subject to tempered stable noise

We test the consequences of noise applied to zero or normal modes via the following selections:

(i) $\gamma_0^{(B)} = \gamma_0^{(R)} = 0$, $\gamma_r^{(B)} = \gamma_s^{(R)} = 1$, $\{r, s\} \in \{\mathscr{B}^E/\{0\}, \mathscr{R}^E/\{0\}\}$ has noise applied to normal modes;

(ii) $\gamma_0^{(B)} = \gamma_0^{(R)} = 1$, $\gamma_r^{(B)} = \gamma_s^{(R)} = 0$, $\{r, s\} \in \{\mathscr{B}^E/\{0\}, \mathscr{R}^E/\{0\}\}$ has noise applied to zero modes.

These choices then specify the random variables in the stochastic system. In the full problem of noise applied generally, there are three sets of random variables, two vector and one scalar, corresponding to the deterministic variables $(\vec{x}, \vec{y}, \Delta)$. These correspond to blue and red Laplacian projections and the phase difference between centroids.

We consider first the case $\gamma_0^B = \gamma_0^R = 0$ where Lévy noise is introduced on normal mode fluctuations on the background of the deterministic Δ. The latter is governed by the solution (29) which tends to a fixed value as $t \to \infty$ or is periodic, according to the sign of $\mathscr{K}$ in Eq. (30). We show in the following how with tempered Lévy noise this devolves to a system we have solved elsewhere [44]; we will not give the solution here but explain the behavior it implies and why it is less interesting than the zero mode case.

As Δ is no longer a random variable, in this case, all the normal mode Langevin equations in Eq. (34) are independent. We may therefore consider the fractional version of a Langevin equation for the blue modes x_s [the corresponding equations for y_s are easily translated from Eq. (34)]:

$$\dot{x}_s = q_s^{(B)}(x_s, \Delta) + \dot{L}_s^{\alpha,\theta,\lambda}(t), \tag{41}$$

where $L^{\alpha,\theta,\lambda}(t)$ is a tempered stable Lévy process in time described by parameters α, θ, λ. For ease of notation, we will first take the noise as if applied within the normal mode projected system, and translate back to the original basis subsequently. Because in the approximation that off-diagonal entries of the super-Laplacian are taken to be zero, the u_j in Eq. (33) are, for the blue system, the eigenvector components $e_j^{(B,r)}$, $j = 1, \ldots, N$.

Thus, the corresponding Fokker-Planck equation can be decomposed into a product of $N + M - 2$ densities

$$\mathscr{P}(\vec{x}, \vec{y}, t) = \prod_{r \in \mathscr{B}^E/\{0\}} \mathscr{P}^{(B,r)}(x_r, t) \prod_{s \in \mathscr{R}^E/\{0\}} \mathscr{P}^{(R,s)}(y_s, t)$$

leading to a decoupling into separate fractional Fokker-Planck equations for each mode.

The probability density $\mathscr{P}(x, t)$ associated with the tempered-stable Lévy process given by Eq. (41) satisfies the fractional Fokker-Planck equation [45]

$$\frac{\partial}{\partial t}\mathscr{P}^{(B,r)}(x, t) = \left\{\sigma^2 \partial_{x_r}^{\alpha,\theta,\lambda} - \frac{\partial}{\partial x_r} q_r^{(B)}(x_r, t)\right\} \mathscr{P}^{(B,r)}(x_r, t), \tag{42}$$

$$\mathscr{P}^{(B,r)}(x_r, 0) = \delta(x_r - x_r'), \tag{43}$$

where $\sigma^2 \in (0, \infty)$ is the diffusion constant, which becomes the variance of the process in the Gaussian limit. Unpacking $q_r^{(B)}$ gives the explicit form of the tempered-fractional Fokker-Planck equation (TFFP) for the normal mode projection of the blue-vs-red system

$$\begin{aligned}\frac{\partial}{\partial t}\mathscr{P}^{(B,r)}(x_r, t) = \Big\{&\sigma^2 \mathscr{D}_{x_r}^{\alpha,\theta,\lambda} + \big[\zeta_B \lambda_r^{(B)} x_r + \sigma^2 \upsilon^{\alpha,\theta,\lambda} \\ &- \big(\omega^{(r)} - \zeta_{BR} d_r^{(BR)} \sin[\Delta(t) - \phi]\big)\big] \frac{\partial}{\partial x_r} \\ &+ \big[\zeta_B \lambda_r^{(B)} + \sigma^2 \upsilon^{\alpha,\lambda}\big]\Big\} \mathscr{P}^{(B,r)}(x_r, t).\end{aligned} \tag{44}$$

For the Gaussian limit, i.e., $\partial_x^{\alpha,\theta,\lambda} = \frac{\partial^2}{\partial x^2}$, Sec. 1.8.3.6 of [46] gives a set of nonlinear transformations which result in

the Gaussian equivalent of Eq. (44) becoming the standard heat equation. Indeed, this technique enabled the analytical investigation of clustering effects in the frustrated Kuramoto model under the influence of Gaussian white noise [8].

As alluded several times, we have solved a version of this problem in [44] where the sign of $\mathscr{K}$ and the shape of the underlying noise distribution interplay in determining the solution. For $\mathscr{K} > 0$, where Δ asymptotes to a constant value, the probability density broadens from a delta function to a tempered stable density of corresponding characteristics given by α, θ, λ. For $\mathscr{K} < 0$, where Δ becomes oscillatory, the Fokker-Planck density evolves from the delta function to a tempered stable density of *fixed shape* (again, according to α, θ, λ) but whose center oscillates according to the dynamics of Δ. This is a natural generalization of the behavior seen for the Gaussian case in [8].

These behaviors will result in corresponding dynamics for the order parameters $O_B(t)$ and $O_R(t)$ for weak values of σ. For $\mathscr{K} > 0$, these will exhibit noisy behavior (showing tempered heavy tails) around a steady-state value, while for $\mathscr{K} < 0$ there will be similar noisy behavior around an oscillatory background. Importantly, if noise is applied across all nodes independently, we expect a residual imprint of the sign of $\mathscr{K}$ in the dynamics. In this respect, there is little that is surprising in the normal modes and so we turn to the potentially more interesting case of the zero modes.

B. Noisy zero modes

Taking $\gamma_i = 0$ and $\gamma_0 = 1$, we consider the tempered fractional Fokker-Planck equation with the tilted ratchet potential from Langevin form (36) and wrap their densities $\mathscr{P}(x,t)$ onto $\mathbb{S}^1$.

It is straightforward using the probability density to compute the mean and variance of Δ which are shown in Fig. 1 for $\phi = 0.96\pi$ and 0.94π, across the threshold between blue and red deterministically locking or drifting. However, we may also derive dynamical properties such as the average velocity $\dot{\Delta}$ drawing upon [47]. From Eq. (43) we obtain that each population density can be rewritten in terms of the *probability current* $\mathscr{J}(x,t)$ as

$$\frac{\partial}{\partial t}\mathscr{P}(x,t) + \frac{\partial}{\partial x}\mathscr{J}(x,t) = 0 \tag{45}$$

$$\Rightarrow \mathscr{J}(x,t) = -\left\{\sigma^2 \partial_x^{\alpha,\theta,\lambda} + \frac{\partial}{\partial x}V'(x)\right\}\mathscr{P}(x,t). \tag{46}$$

We now restrict the support of x to $\mathbb{S}^1$ by constructing the so-called *reduced density* $\mathscr{P}^{(\mathrm{reduc})}(x,t)$ and *reduced probability current* $\mathscr{J}^{(\mathrm{reduc})}(x,t)$ through

$$\begin{aligned}\mathscr{P}^{(\mathrm{reduc})}(x,t) &\equiv \sum_{n=-\infty}^{\infty}\mathscr{P}(x+2\pi n,t),\\ \mathscr{J}^{(\mathrm{reduc})}(x,t) &\equiv \sum_{n=-\infty}^{\infty}\mathscr{J}(x+2\pi n,t).\end{aligned} \tag{47}$$

Due to the linearity of the Fokker-Planck equation, the reduced density and reduced probability current also obey Eq. (46) but with the new boundary and normalization conditions

$$\mathscr{P}^{(\mathrm{reduc})}(-\pi,t) = \mathscr{P}^{(\mathrm{reduc})}(\pi,t), \qquad \int_{-\pi}^{\pi}\mathscr{P}^{(\mathrm{reduc})}(x,t)dx = 1. \tag{48}$$

Just like the Gaussian case [43], we expect that for tempered stable Lévy noise the steady-state equivalent of Eq. (43) with vanishing boundary conditions at the natural boundaries $x \to \pm\infty$ will be non-normalizable due to metastability. The steady state density $\mathscr{P}_{st}^{(\mathrm{reduc})}(x)$ on $\mathbb{S}^1$ satisfies

$$\left\{\sigma^2\partial_x^{\alpha,\theta,\lambda} + \frac{\partial}{\partial x}V'(x)\right\}\mathscr{P}_{st}^{(\mathrm{reduc})}(x) = 0 \tag{49}$$

with boundary and normalization conditions given by Eq. (48).

The solution is obtained by Fourier transformation of Eq. (49) revealing the expression

$$\begin{aligned}&\widehat{Q}(k+1) = -f_k\widehat{Q}(k) + \widehat{Q}(k-1),\\ &\text{where}\quad \widehat{Q}(k) \equiv e^{-ik\rho}\,\widehat{\mathscr{P}}_{st}^{(\mathrm{reduc})}(k),\\ &\text{and}\quad f_k \equiv -\frac{2}{k\sqrt{S^2+C^2}}[\Lambda(k) + ik\mu],\end{aligned} \tag{50}$$

and we note that because of periodicity, the Fourier variables k are integer valued. We can then construct the corresponding reduced probability density via the discrete inverse Fourier transform

$$\mathscr{P}_{st}^{(\mathrm{reduc})}(x) = \frac{1}{2\pi}\left\{\widehat{Q}(0) + 2\mathbb{R}\sum_{n=1}^{\infty}e^{-in(x-\rho)}\widehat{Q}(n)\right\}, \tag{51}$$

where $\widehat{Q}(0) = 1$ from the normalization condition in Eq. (48). The remaining $\widehat{Q}(n)$ may be solved via the nonlinear transform

$$S_{k+1} = \frac{\widehat{Q}(k+1)}{\widehat{Q}(k)}, \tag{52}$$

which transforms the linear three-term recurrence relation given by Eq. (50) into the following nonlinear two-term recurrence relation:

$$S_k = \frac{1}{f_k + S_{k+1}}. \tag{53}$$

Equation (53) can be solved iteratively with the application of continued fractions

$$S_k = \frac{1}{f_k + \frac{1}{f_{k+1}+S_{k+2}}} = \frac{1}{f_k + \cfrac{1}{f_{k+1}+\cfrac{1}{f_{k+2}+\cfrac{1}{\ddots}}}}$$

whose values can be used to reconstruct the corresponding $\widehat{Q}(k)$ expressions using

$$\widehat{Q}(k) = S_k S_{k-1}\ldots S_2 S_1\widehat{Q}(0) \tag{54}$$

for insertion into Eq. (51).

In this paper, we mainly focus on the average velocity $\langle\dot{\Delta}\rangle$, which is defined through the reduced steady-state probability current $\mathscr{J}_{st}^{(\mathrm{reduc})}(x)$ with x replaced by Δ as follows:

$$\langle\dot{\Delta}\rangle = \frac{d}{dt}\langle\Delta\rangle = \int_{-\pi}^{\pi}\mathscr{J}_{st}^{(\mathrm{reduc})}(\Delta)d\Delta. \tag{55}$$

Nonzero values of $\langle\dot{\Delta}\rangle$ indicate that through a combination of drift and noise there is a rotation of the centroid of blue with respect to that of red; positive values mean that blue advances and negative values mean that red advances. The average velocity $\langle\dot{\Delta}\rangle$ is solved for giving

$$\langle\dot{\Delta}\rangle = \begin{cases} -\frac{\sigma^2\alpha\theta\lambda^{\alpha-1}}{\cos\left(\frac{\pi\alpha}{2}\right)} + \mu - 2\pi\gamma\mathbb{I}\{\widehat{Q}(1)\}, & 0 < \alpha < 1 \\ \mu - 2\pi\gamma\mathbb{I}\{\widehat{Q}(1)\}, & 1 < \alpha < 2. \end{cases} \tag{56}$$

We now need to take into account the Laplacian projection of the noise. It is straightforward to see that as the equation for Δ arises from the difference $B - P$, the $N + M$ components of u_j in Eq. (33) for this purpose are

$$u_j = \begin{cases} \frac{1}{\sqrt{N}}, & j = 1, \ldots, N \\ -\frac{1}{\sqrt{M}}, & j = N+1, \ldots, N+M. \end{cases} \tag{57}$$

Equation (33) thus gives

$$\begin{aligned} \Lambda_0(k) = \sigma^2 \Bigg\{ & (1+\theta)\left[N\left(\lambda + \frac{ik}{\sqrt{N}}\right)^{\alpha} + M\left(\lambda - \frac{ik}{\sqrt{M}}\right)^{\alpha}\right] \\ & + (1-\theta)\left[N\left(\lambda - \frac{ik}{\sqrt{N}}\right)^{\alpha} + M\left(\lambda + \frac{ik}{\sqrt{M}}\right)^{\alpha}\right] \\ & - ik(\sqrt{N} - \sqrt{M})v^{\alpha,\theta,\lambda} + (N+M)v^{\alpha,\lambda} \Bigg\}. \end{aligned} \tag{58}$$

Noting that in the explicit example we consider, $N = M$, this leads to

$$\Lambda_0(k) = 2\sigma^2 N\left[\left(\lambda + \frac{ik}{\sqrt{N}}\right)^{\alpha} + \left(\lambda - \frac{ik}{\sqrt{N}}\right)^{\alpha} + v^{\alpha,\lambda}\right]. \tag{59}$$

This can be further simplified to

$$\begin{aligned} \Lambda_0(k) = & 2\sigma^2 N^{1-\alpha/2}[(\sqrt{N}\lambda + ik)^{\alpha} \\ & + (\sqrt{N}\lambda - ik)^{\alpha} + v^{\alpha,\sqrt{N}\lambda}]. \end{aligned} \tag{60}$$

We see that for the mode Δ, the parameters of the noise H for the zero mode projected system are a simple rescaling of those of the noise η on the original system:

$$\sigma^2 \to \sigma^2 N^{1-\alpha/2}, \tag{61}$$

$$\lambda \to \sqrt{N}\lambda, \tag{62}$$

$$\theta \to 0. \tag{63}$$

Significantly, both the tempering and noise strength are *enhanced*, and the skew is *eliminated*. The interplay of these for various α and λ are not easily read off from Eq. (56).

In the bottom row of Fig. 1 we show the λ dependence of $\langle\dot{\Delta}\rangle$ for various α from Eq. (56) for the couplings in Eqs. (40) and with $\phi = 0.96\pi$, $\psi = 0$ (left, for which $\mathscr{K} < 0$, o there is drift) and $\phi = 0.94\pi$, $\psi = 0$ (right, for which $\mathscr{K} > 0$, or the system locks). Note that for all of these plots we use $\sigma = 0.1$, a slightly larger value than used for simulations as this makes the effects visible for all the properties across a common scale. We stress that these are all computed for steady state, *not static*, reduced distributions in the ratchet potential.

In all cases, we see several common broad features. Whereas $\langle\Delta\rangle$ is positive, $\langle\dot{\Delta}\rangle$ is nonzero and negative. This is why we emphasized earlier that a nonzero steady-state average does not imply static behavior, so that the average of Δ needs to be interpreted cautiously. It suggests that although blue succeeds on average in locking ahead of red, there is drift with red advancing in relation to blue. This appears to have a knock-on effect that the average Δ is generally smaller for the deterministically drifting case (left hand panels) than for the deterministically locked case (right hand panels), even though the average velocity is generally larger for the former. In other words, when there is more drift, Δ does not settle into a value that recurs more frequently, and therefore a larger average value does not develop.

We see in all cases that the near Gaussian case (red curve) is correctly λ independent. The curves on the top, for $\phi = 0.96\pi$, represent generally larger absolute values of $\langle\dot{\Delta}\rangle$, consistent with $\mathscr{K} < 0$ so that deterministic dynamics already implies $\dot{\Delta} \neq 0$. Tempering in general reduces the variance and average velocity.

There are key differences across the plots. Significantly, for the average Δ the impact of tempering is strongest for values of $\alpha < 1$. For both values of ϕ we observe that tempering leads to more suppression of variance for $\alpha < 1$.

For small tempering λ the average velocity is larger in absolute magnitude for smaller α (though difficult to discern on this scale), but there is a critical value of λ at which this behavior reverses, with small α values seeing more suppression. However, the effect eventually flattens out as λ increases. Thus, even when deterministically there is drift between clusters, as in $\phi = 0.94\pi$ on the left, tempered stable noise with small α and large tempering λ can cancel some of the diffusive drift. For $\phi = 0.96\pi$, on the right, the black curve here for $\alpha = 0.3$ genuinely approaches zero. Thus, for small α and sufficient tempering λ, the noise induced drift between blue and red may be canceled entirely.

To summarize the key insights from this section: For small α in the presence of tempering, there is a greater suppression of the average phase difference between blue and red, and its variance. The noise may also diminish the drift between blue and red clusters even when deterministically they might otherwise be in relative motion. For the deterministically locked situation, noise may be canceled entirely. Although we have not yet drawn attention to it, this behavior is independent of the graph structure of blue and red since it arises purely from the structure of the fixed point as represented in the potential $V(\Delta)$ in Eq. (24).

V. NOISY BEHAVIOR IN THE FULL DYNAMICS

We now focus on investigating the full nonlinear dynamics of the stochastic blue vs red model using numerical simulations. The aim of this numerical investigation is to identify the optimal internal synchronization and phase lag of the blue network against the red network and to understand how the noise parameters α, σ, and λ lead to either steady, periodic, or noisy pathwise behavior.

A. Implementation

To simulate the full tempered fractional stochastic blue-vs-red model, we implemented code in C++ for maximum performance and used the Messaging Passing Interface (MPI) to parallelize the simulation across an arbitrary number of CPU cores. The simulation is performed using a Euler method to simulate the dynamics at the N vertices. This algorithm was chosen as it allows the code to easily switch between the cases of (1) no noise, (2) Gaussian noise, (3) stable noise, or (4) tempered stable noise without changing the underlying algorithm. The code takes the following parameters: the noise distribution parameters; the number of paths to simulate; the number of time steps in each path; and the filename containing the graph $\mathcal{G}$ stored in graph6 format [48]. The code also includes a number of hand-implemented random sampling algorithms for stable and tempered stable distributions. The evaluation of the expected values of the order parameter is approximated through a simple Monte Carlo procedure, that is, we approximate the expected value of the order parameter upon the discretizations $\mathbb{E}[(O_B)_i] = \mathbb{E}[(O_B(t_i)],\ t_i \in [0, T],\ i = 1, \ldots, N$ through the mean $(\bar{O}_B)_i = \frac{1}{M}\sum_{m=1}^{M}(O_B)_i^{(m)}$ where $(O_B)_i^{(m)}$ is the ith discretized value of the mth simulated path of the order parameter O_B. From the central limit theorem we have that

$$(\bar{O}_B)_i \sim \mathcal{N}\left(\mathbb{E}[(O_B)_i], \frac{s}{\sqrt{M}}\right), \tag{64}$$

where $\mathcal{N}$ is the normal distribution and the standard deviation of the order parameter estimate is given as $s = \frac{1}{M-1}\sum_{m=1}^{M}[(O_B)_i^{(m)} - (\bar{O}_B)_i]^2$. This is similarly done for $(O_B)_i$ and Δ_i.

B. Pathwise dynamics

In the following, we show the pathwise dynamics, namely, individual but characteristic instances, for tempered stable Lévy noise choices for cases where we have previously examined the deterministic [7] and Gaussian noise [8] systems. We first focus on the dynamics for specific values of σ, α, λ while always using the one-sided case $\theta = 1$. We generate time series of the order parameters O_B, O_R, and Δ. We choose values where both deterministic and stochastic properties are evident, in other words, where noise is not dominant. In most cases, this limits us to choices $\alpha > 1$ so we use $\alpha = 1.5$ as a value sufficiently far from Gaussian. Our choice of points in the (ϕ, ψ) landscape will be both below and above the threshold $\mathcal{K} = 0$. These should be compared to corresponding plots for the Gaussian case in [8]. We note that whereas in that work we plotted box-whisker charts for the data at each time step, here we simply plot the mean and the standard deviation on a dual axis. Thus, the fluctuations in O_B and O_R may appear to exceed unity: this is an artifact of how we represent the deviations.

To begin with, we consider stable noise for $\sigma = 0.05$ and $\alpha = 1.5$ in Fig. 2.We show examples for four points in the (ϕ, ψ) plane, two below, one at the threshold of $\mathcal{K} = 0$, and the other above. We observe, first, that levels of synchronization in O_B and O_R are high in all cases, however, the nature of the fluctuations can be quite different. While $\mathcal{K} > 0$, as for the top two cases, the fluctuations are quite random about a constant mean. The heavy-tail jumps are more evident in Δ in contrast to O_B, O_R. Below $\mathcal{K} = 0$, as for $\phi = 0.96\pi,\ \psi = 0$ a clear periodicity is evident in all measures, however, for O_B and O_R the superimposed jumps are also marked. These should be contrasted with a far more incremental stochasticity in the Gaussian case shown in [8]. The behavior of Δ in the fourth instance is quite telling: the periodicity is evident, however, after each cycle there is a distortion in the period that incrementally increases.

The important point to emphasize is that we are applying noise here to all nodes so that we are stimulating in essence both the zero and normal modes according to the Laplacian. Nevertheless, we can distinguish the impact on the two classes of mode quite cleanly. First, the dominance of the periodicity when $\mathcal{K} < 0$ with noise superimposed is a consequence of the noise on *normal modes* but the underlying deterministic behavior of the zero mode, namely $\Delta(t)$, leaving its mark. Second, the stochasticity in the periodicity itself of Δ when $\mathcal{K} < 0$ is a consequence of the noise on the zero mode itself. Specifically, the Lévy ratchet potential manifests itself in the probabilistic nature of how long the system stays in the metastable well when subject to noise. We recall from [8] that when Gaussian noise is only applied to normal modes, the behavior of $\Delta(t)$ in the $\mathcal{K} < 0$ regime is strictly periodic.

In light of this discussion, understanding the tempered case is straightforward. Shown in Fig. 3, we observe essentially the same characteristics but with moderation of the stochasticity. Tempering here is at $\lambda = 0.75$ so that the jumps in O_B and O_R are significantly smaller and sparser, both for constant and periodic behaviors. In the behavior of Δ, the broadening for $\mathcal{K} > 0$ is smoother. For the periodic regime $\mathcal{K} < 0$, the period is far more well defined as a consequence of the stabilization of the system in the ratchet potential.

We have avoided thus far to show results for $0.5 < \alpha < 1$ as there is little structure distinguishable due to the heaviness of the tails. However, in the presence of tempering with $\alpha = 0.5$, recognizable structures emerge as shown in Fig. 4. We see here the behavior predicted analytically that with tempering and small values of α a smoother dynamics is restored.

C. Objective function for deterministic system

We now focus on the fitness landscape, where fitness refers to optimal *internal synchronization and phase lag* for one population with respect to the other; we choose blue for this purpose. To this end, we choose an objective function given by

$$U(\phi, \psi) = \left(\sum_{i=1}^{3} w_i U_i\right)^{-\frac{1}{4}}, \tag{65}$$

where w_i are the weights of subobjective functions U_i. These subobjective functions, upon the discretizations

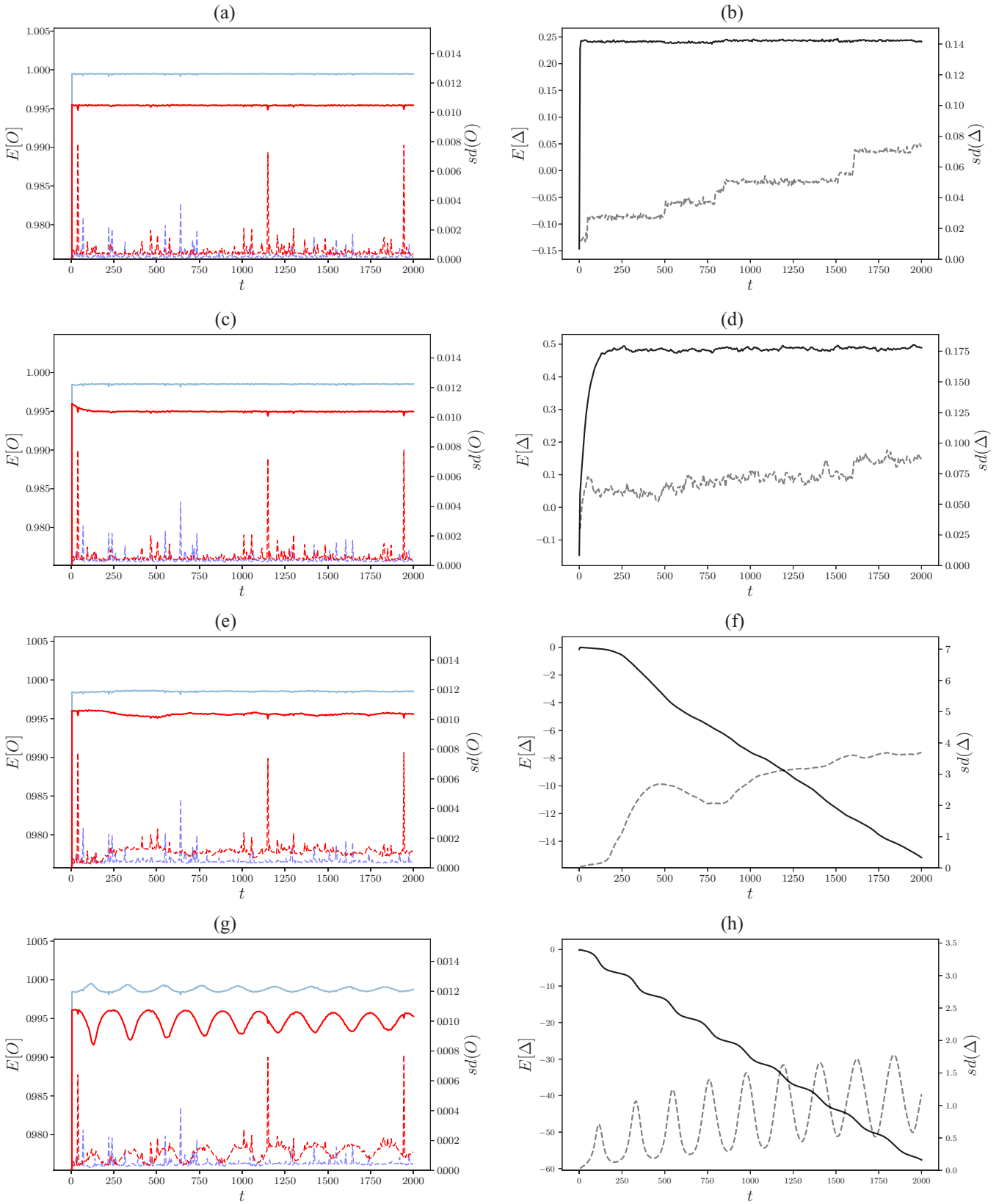

FIG. 3. Time series plots in the stable Lévy noise case with $\sigma = 0.05$ and $\alpha = 1.5$ and $\lambda = 1$. Left axis: time series plots for the average order parameters and Δ. Right axis: time series plots (dashed lines) for the standard deviation of the Monte Carlo estimates of the order parameters and Δ. Left column: order parameters for the blue and red networks as given by the blue (light gray) and red (gray) lines, respectively. Right column: Δ as denoted by the black lines. (a), (b) $(\phi, \psi) = (0.2\pi, 0)$; (c), (d) $(\phi, \psi) = (0.94\pi, 0)$; (e), (f) $(\phi, \psi) = (0.95\pi, 0)$; (g), (h) $(\phi, \psi) = (0.96\pi, 0)$.

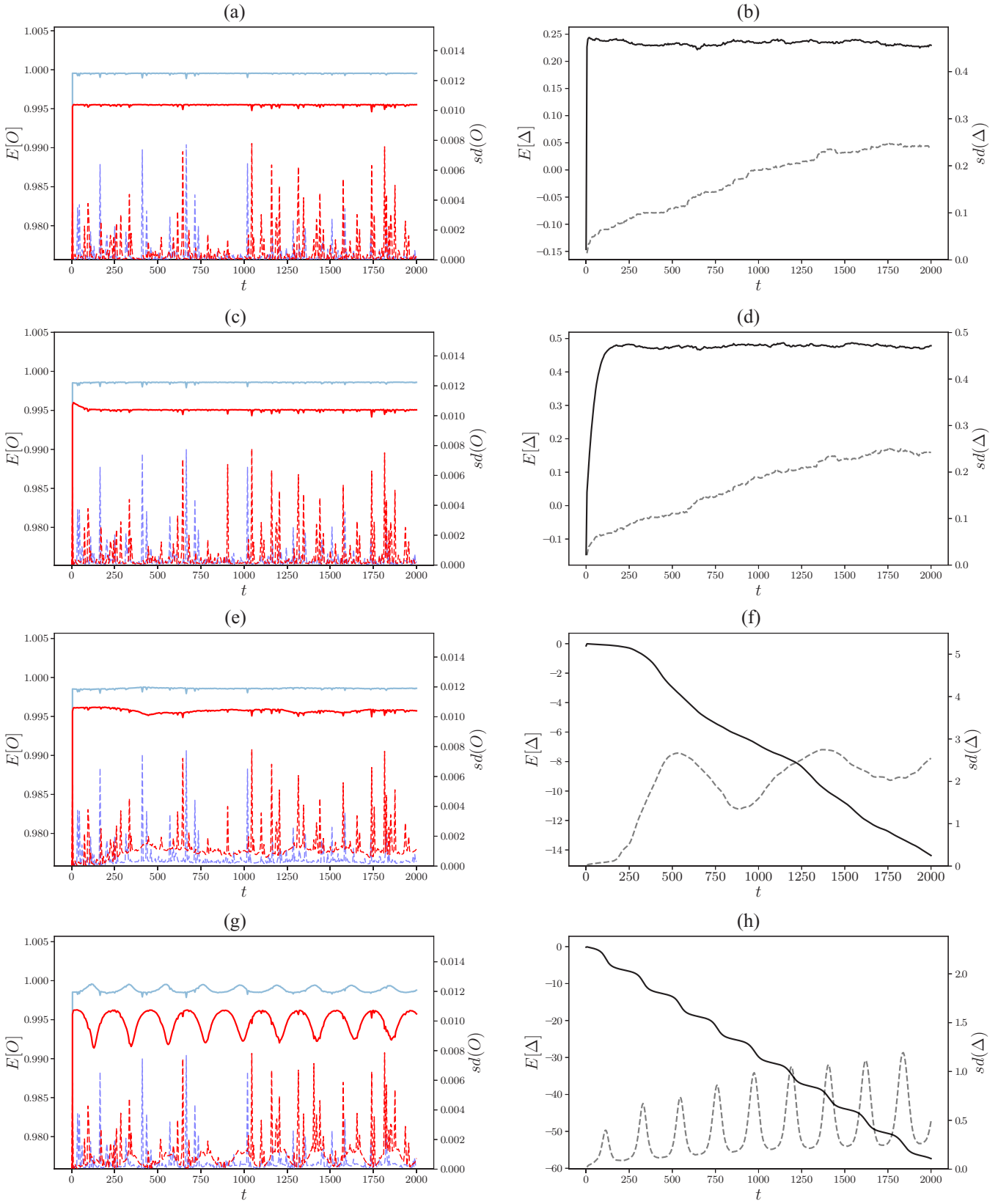

FIG. 4. Time series plots in the stable Lévy noise case with $\sigma = 0.05$ and $\alpha = 0.5$ and $\lambda = 0.75$. Left axis: time series plots for the average order parameters and Δ. Right axis: time series plots (dashed lines) for the standard deviation of the Monte Carlo estimates of the order parameters and Δ. Left column: order parameters for the blue and red networks as given by the blue (light gray) and red (gray) lines, respectively. Right column: Δ as denoted by the black lines. (a), (b) $(\phi, \psi) = (0.2\pi, 0)$; (c), (d) $(\phi, \psi) = (0.94\pi, 0)$; (e), (f) $(\phi, \psi) = (0.95\pi, 0)$; (g), (h) $(\phi, \psi) = (0.96\pi, 0)$.

$(O_B)_i = O_B(t_i)$, $t_i \in [0, T]$, $i = 1, \ldots, N$, and similarly for $(O_R)_i$ and α_i, are given by

$$U_1 = \sqrt{\sum_{i=1}^{N}[(O_B)_i - 1]^2} + \sqrt{\sum_{i=1}^{N}\left[\frac{d}{dt}(O_B)_i - 0\right]^2}, \quad (66)$$

$$U_2 = \sqrt{\sum_{i=1}^{N}(\Delta_i - \phi)^2}, \quad (67)$$

$$U_3 = \sqrt{\sum_{i=1}^{N}\left[\frac{d}{dt}(O_R)_i - 0\right]^2}, \quad (68)$$

where U_1, U_2, and U_3 correspond to O_B being constant and close to 1, Δ being close to ϕ, and O_R being constant, respectively. We indicate the value of 0 in Eq. (66) to emphasize that objective function seeks constant O_B and O_R. This choice of combination of U_1, U_2, and U_3 captures the tradeoffs required by the blue agents to maintain both stable internal synchronization $O_B = 1$, $\dot{O}_B = 0$, and maintain a lead in the cycle ϕ over the competitor, red, namely, $\Delta = \phi$. We also include a requirement that red have static value of the order parameter O_R, without seeking it to be close to 1. In other words, blue prefers to be internally well synchronized, and red at best frequency synchronized but to the extent that blue agents interacting with red may achieve a phase advantage of ϕ. The choice of the power $-\frac{1}{4}$ in Eq. (65) is for visualization purposes to enable better resolution of peaks and troughs in the landscape, as will be seen shortly.

D. Bayesian optimization

Instead of performing an exhaustive grid search across the parameters ϕ and ψ over the region $[0, 2\pi] \times [0, 2\pi]$, we approach the problem of finding a global optimum of the various objective functions using the theory of constrained global optimization built upon the ideas of Bayesian inference and Gaussian processes [49,50]. In other words, we seek

$$\max_{\phi,\phi} \{U(\phi, \psi) : \phi, \psi \in [0, 2\pi]\}, \quad (69)$$

using the minimal number of probes of $U(\phi, \psi)$. One of the consequences of this approach is that we may obtain a view of the fitness landscape by interpolating over the intermediate values obtained by the algorithm as it searches for the global maximum.

Bayesian optimization is different to other kinds of optimization in that it constructs a probabilistic model for seeking the maximum of a function $f(x)$ on some bounded set $\mathcal{X} \subset \mathbf{R}^d$ and then exploits this model to make decisions about where in $\mathcal{X}$ to evaluate next. It uses all of the information available from previous evaluations of $f(x)$ and not simply local gradient and Hessian approximations. This gives an algorithm that finds the maximum of nonconvex functions with relatively few evaluations at the cost of performing more computation to determine the next point to try. This approach is particularly well suited when the evaluation of $f(x)$ is expensive to perform (as in our case). When performing this approach in practice, there are two major implementation choices that need to be made. The first is a model for the prior over functions that express assumptions about the function being optimized. We assume here a Gaussian process prior for the influence of ϕ and ψ on $\mathcal{K}$. Second, the implementation requires a choice of an "acquisition function" used to construct a utility function from the model posterior and allows the algorithm to determine the next point to evaluate. We used the implementation of Bayesian optimization provided by the BAYESOPTIMIZATION package [51].

To improve the performance of the Bayesian optimization algorithm and, in the case of the stochastic system, to account for the standard error of our estimate in Eq. (64), we perform data smoothing on a coarser version of the original data set through the application of a symmetric moving average filtering algorithm. The symmetric moving average filter that we used is of window length $2n + 1$ and is given by

$$(\hat{O}_B)_i = \sum_{j=-n}^{n} \varpi_j \mathbb{E}[(O_B)_i], \quad n < i < N - n \quad (70)$$

where the weights are chosen such that $\sum_j \varpi_j = 1$ and the expectations are approximated through Eq. (64). In our application of this algorithm, we make the simple selection of $\varpi_j = \frac{1}{2n+1}$. For the n observations at the beginning and end of the time series, we use an asymmetric moving average filter to preserve all observations. Unless otherwise stated, we use $n = 10$ in our window length.

E. Fitness landscape for deterministic system

In the top panel of Fig. 5 we show the objective function for the deterministic system in the ϕ, ψ plane. We compare it below with a plot of the objective function but with only the term corresponding to w_1 included, where we evaluate $O_B(\phi, \psi)$ based on the truncation to lowest order in the fixed point approximation (37), as discussed earlier. In addition, we overlay on this latter plot the lines (in black) where $\mathcal{K} = 0$.

In the top panel of Fig. 5, we observe an overall "ridge" of optimality in the bright strip on the diagonal, and, with same alignment, dark narrow troughs far from optimality. This ridge, however, sits at the top of a similarly aligned region that drops off orthogonally to the bright ridge down to the darkly colored troughs. Correspondingly, the overall symmetry of the objective function on the top is displayed in the truncated form of O_B below. We may infer that the negatively sloped diagonal of maxima and minima in the top panel is a consequence completely of the behavior of $\mathcal{K}$ shown in the lower plot. Because of the specific small choice of μ in our example, the region where $\mathcal{K} < 0$ (where the angle between blue and red centroids, Δ, becomes time dependent) is very narrow, in the narrow gap between the black lines in the bottom plot. This is, therefore, responsible for the narrow troughs in the objective function on the top. Similarly, where the objective function takes its maximum coincides at points with where $\mathcal{K}$ achieves its maximum positive value, as well as O_B itself as seen periodically along the central diagonal of the lower plot.

However, something difficult to detect in a single quantity such as used in O_B on the bottom but evident in the full objective function on the top is that it is impossible for blue to achieve the *combined objective* of optimal internal synchronization *and* large frustration in relation to red, ϕ, for a fixed value of red's frustration in relation to blue. This is visible in the top plot as follows. On the one hand, following the bright

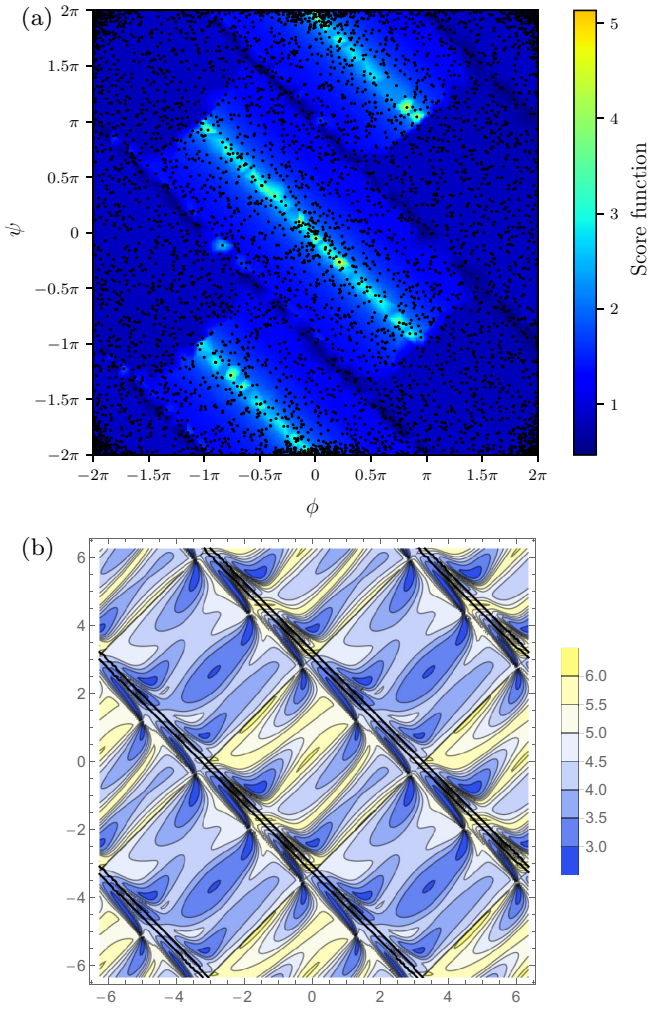

FIG. 5. (a) Objective score function for $U(\phi, \psi)$ in the deterministic case with 500 iterations and $T = 1000$. The objective weights are given by $w_1 = 1$, $w_2 = 0$, and $w_3 = 1$. High scoring (red) values correspond to O_B constant and close to 1 and O_R constant while low scoring values (blue) correspond to either periodicity or noisy behavior in the times series or O_B far away from 1. Note that the optimal value near $(1.1\pi, 1.85\pi)$ in this fitness landscape corresponds to a periodic time series with a very long periodicity, beyond that of $T = 1000$. The subsequent plot repeats the construction of the fitness landscape for $T = 2000$. (b) The objective function including only the analytical evaluation of O_B truncating to leading order in the fixed point. This is overlaid in black with the lines where $\mathscr{K} = 0$.

ridge of the plot, positive values of ϕ require negative values of ψ to maintain high optimality. This ridge corresponds to red being "compliant" with blue's intent: large positive phase ϕ for blue is consistent with large negative phase $-\phi$ for red. However, these bands do not extend indefinitely along the diagonals of the (ϕ, ψ) plane but are truncated. This is a consequence of the presence of U_2 in the objective function (66) where optimality requires a sign of Δ: blue seeks to be a certain phase *ahead* of red. This truncation of the diagonal band is only seen partially in the bottom plot in that the central cell is a square rather than a rectangle in the upper plot.

Once values of (ϕ, ψ) off the diagonal are chosen, the degree of optimality drops off into rectangular bands that align with the diagonal ridge. This dropoff is a consequence of the combination of internal synchronization *and* achievement by blue of maintaining close to the phase difference ϕ ahead of red, but where red chooses "noncompliant" values ψ. The larger is $\psi > 0$, the smaller the range of $\phi > 0$ available before instability occurs, namely, a dark ridge in the plot is encountered. Thus, this landscape representation summarizes the tradeoffs in internal synchronization and ability to synchronize in a stable manner ahead of the competitor available to one side or the other given the choices of the other. The question we address next is how much of this structure is maintained in the presence of stable and tempered stable noise.

F. Fitness landscape for stochastic system

To study the fitness landscape in the presence of noise, we use the objective function of Eq. (65) but with subobjective functions using the discretizations $(\hat{O}_B)_i = \hat{O}_B(t_i)$, $t_i \in [0, T]$, $i = 1, \ldots, N$, and similarly for $(\hat{O}_R)_i$ and $(\hat{\Delta})_i$, are given in terms of the smoothed expected values as defined in Eq. (70). The subobjective functions then are as follows:

$$U_1 = \sqrt{\sum_{i=1}^{N}[(\hat{O}_B)_i - 1]^2} + \sqrt{\sum_{i=1}^{N}\left[\frac{d}{dt}(\hat{O}_B)_i - 0\right]^2}, \quad (71)$$

$$U_2 = \sqrt{\sum_{i=1}^{N}[(\hat{\Delta})_i - \phi]^2}, \quad (72)$$

$$U_3 = \sqrt{\sum_{i=1}^{N}\left[\frac{d}{dt}(\hat{O}_R)_i - 0\right]^2}, \quad (73)$$

where U_1, U_2, and U_3 correspond to $\hat{O}_B$ being constant and close to 1, $\hat{\Delta}$ being close to ϕ, and $\hat{O}_R$ being constant, respectively.

In Fig. 6 we show four cases of the objective function, comparing the deterministic, Gaussian (top left and right), and, importantly, the stable case for $\alpha = 1.5$ (bottom left) and tempered stable case with $\alpha = 1.5$, $\lambda = 0.5$. In particular, for the two non-Gaussian cases we have used the Bayesian optimization approach.

We observe first that the Gaussian case (top right) maintains to a high degree the integrity of the landscape from the deterministic result. However, stable noise (bottom left), as a consequence of the heavy tails, significantly smears the landscape; we note to this end the change in the color gradations for this case showing that overall values of the objective function are suppressed in comparison to deterministic and Gaussian cases. Also, the accumulation of points searched by the Bayesian optimization underscores the relative suboptimality of (ϕ, ψ) values away from the origin. Nevertheless, the structure of the landscape is maintained. With suppression of the heavy tails by tempering (bottom right), the landscape is closer to the Gaussian case. In Fig. 7 we plot numerical evidence that the optimal fitness landscape results pick out optimal values by plotting the time series of the various order parameters at a point within the optimal band.

In conclusion for this stage, the overall imprint of the deterministic dynamics is retained in non-Gaussian noise cases.

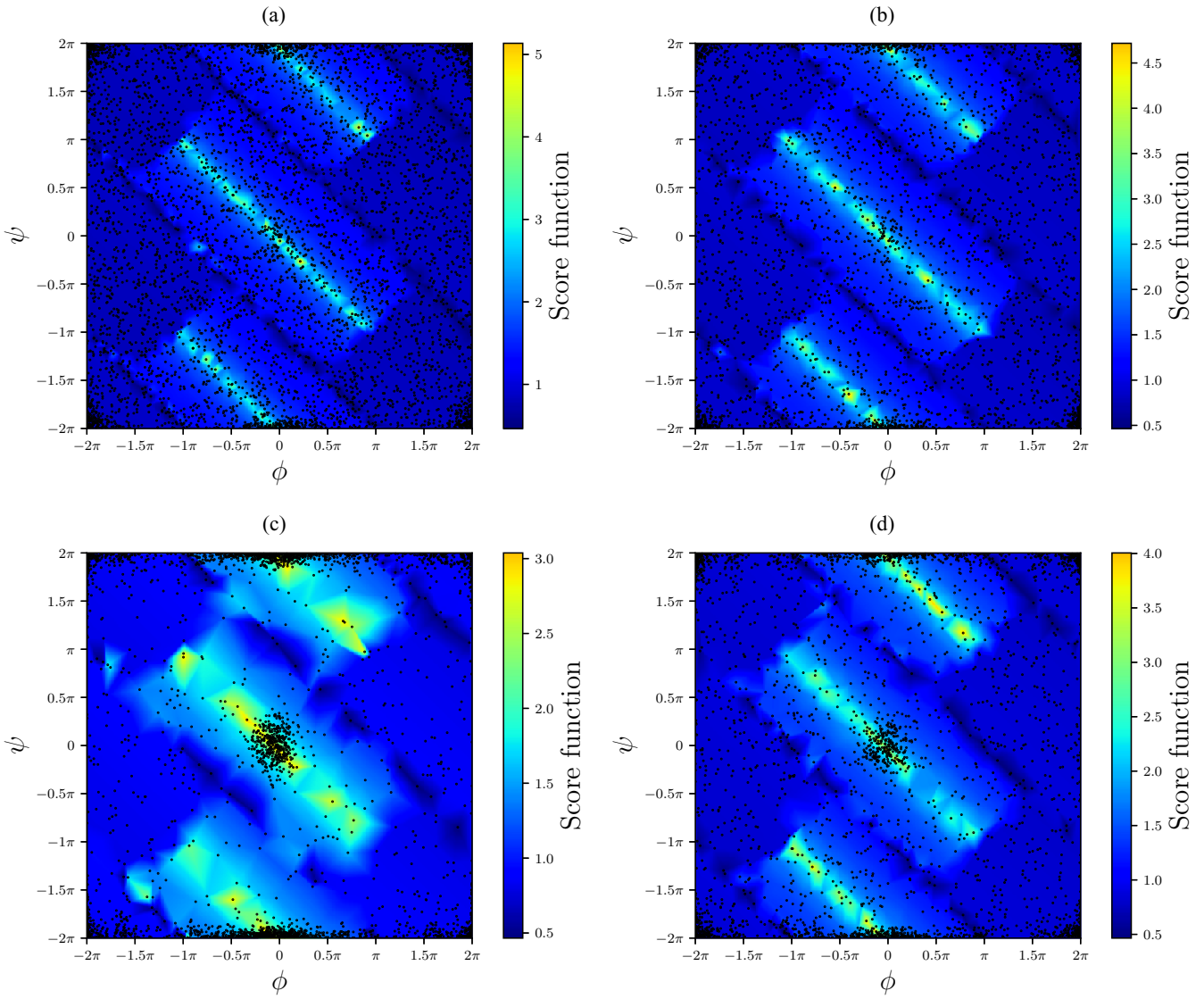

FIG. 6. Objective score function for $U(\phi, \psi)$ for different noise cases: (a) deterministic, (b) Gaussian (top right), (c) stable with $\sigma = 0.05, \alpha = 1.5$, and (d) tempered stable with $\sigma = 0.05, \alpha = 1.5, \lambda = 0.5$, with 500 iterations and $T = 1000$. The objective weights are given by $w_1 = 1,\ w_2 = 0$, and $w_3 = 1$. High scoring (red) values correspond to O_B constant and close to 1 and O_R constant while low scoring values (blue) correspond to either periodicity or noisy behavior in the times series or O_B far away from 1. Note that the optimal value near $(1.1\pi, 1.85\pi)$ in this fitness landscape corresponds to a periodic time series with a very long periodicity, beyond that of $T = 1000$. The subsequent plot repeats the construction of the fitness landscape for $T = 2000$.

In particular, the partition of the (ϕ, ψ) plane according to the sign of $\mathscr{K}$ remains key for determining regions of stochastic optimality.

G. Determining the presence of regular and noisy path behavior

In order to analyze for which values of $(\alpha, \sigma, \lambda)$ the property of periodicity holds, we introduce an objective function

$$U^{(01)}(\alpha, \sigma) = 1 - K, \tag{74}$$

where K is the result of the application of the "0-1 test" upon the $\hat{O}_R$ time series as defined in Eq. (70). The 0-1 test is the means for determining the presence of chaos in time series data that are a computationally efficient alternative to computing a Lyapunov exponent [52,53]. In this work, we shall utilize the 0-1 test to differentiate between regular and noisy path behavior of $\hat{O}_R$. To apply the 0-1 test upon the time series $\hat{O}_R$, we select an observable from the solution $\psi(\hat{O}_R)$ and some parameter $c > 0$. The method used in this test is independent of the form of the function ψ. We now define

$$\theta(t) = ct + \int_0^t \psi(\hat{O}_R) ds, \tag{75}$$

$$p(t) = \int_0^t \psi(\hat{O}_R) \cos(\theta(s)) ds. \tag{76}$$

If the underlying dynamics is regular, then $p(t)$ is bounded otherwise $p(t)$ behaves asymptotically like Brownian motion. To identify the growth of $p(t)$, the mean-square displacement

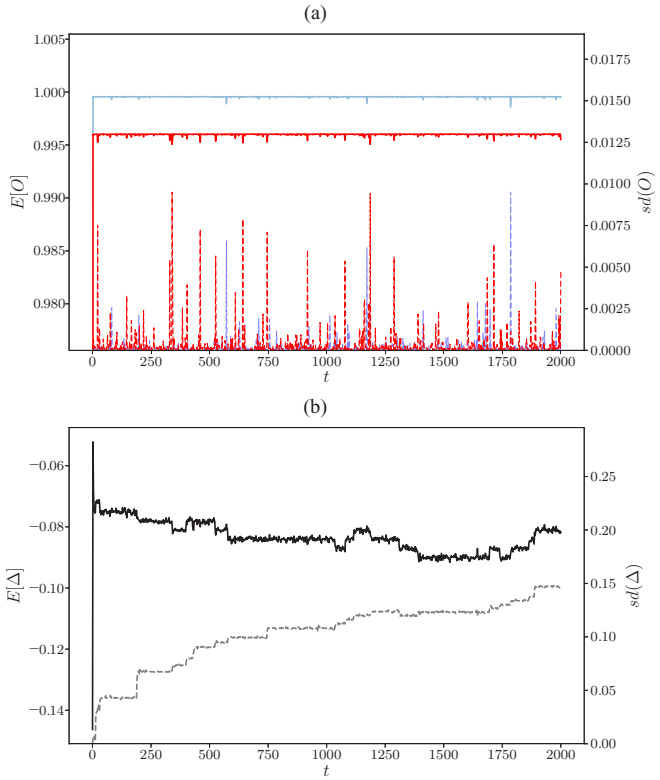

FIG. 7. Time series plots in the optimal regime of $U(\phi, \psi)$ in the tempered stable Lévy noise case with $\sigma = 0.05$, $\alpha = 1.5$, $\lambda = 0.5$ and $(\phi, \psi) = (0, 0)$. Left axis (solid lines): time series plots for the average order parameters and Δ. Right axis (dashed lines): time series plots for the standard deviation of the Monte Carlo estimates of the order parameters and Δ. (a) Order parameters for the blue and red networks as given by the blue (light gray) and red (gray) lines respectively. (b) Δ as denoted by the black lines.

is used:

$$M(t) = \lim_{T\to\infty} \frac{1}{T} \int_0^T [p(t+\tau) - p(\tau)]^2 d\tau. \tag{77}$$

If the behavior $p(t)$ is Brownian, then $M(t)$ will grow linearly in time; otherwise, if $p(t)$ is bounded, then $M(t)$ will be bounded. To distinguish between these two properties, the asymptotic growth rate of the mean-square displacement is calculated:

$$K = \lim_{t\to\infty} \frac{\log(M(t))}{\log t}. \tag{78}$$

This can be calculated through a linear regression of $\log(M(t))$ and $\log t$ and will be near 1 if the underlying dynamics is chaotic or noisy and 0 otherwise. Note that the choice of $1 - K$ in Eq. (74) is the reverse of the typical test, used in this way here for consistency with the landscape plots wherein large values (periodic behavior in the 0-1 test and desired dynamics in the previous objective functions) are "good," and low scoring values (noisy behavior in the 0-1 test and undesired dynamics in the previous objective functions) are "bad."

We now conduct straightforward grid search through the range of parameters in presenting landscape plots. We show

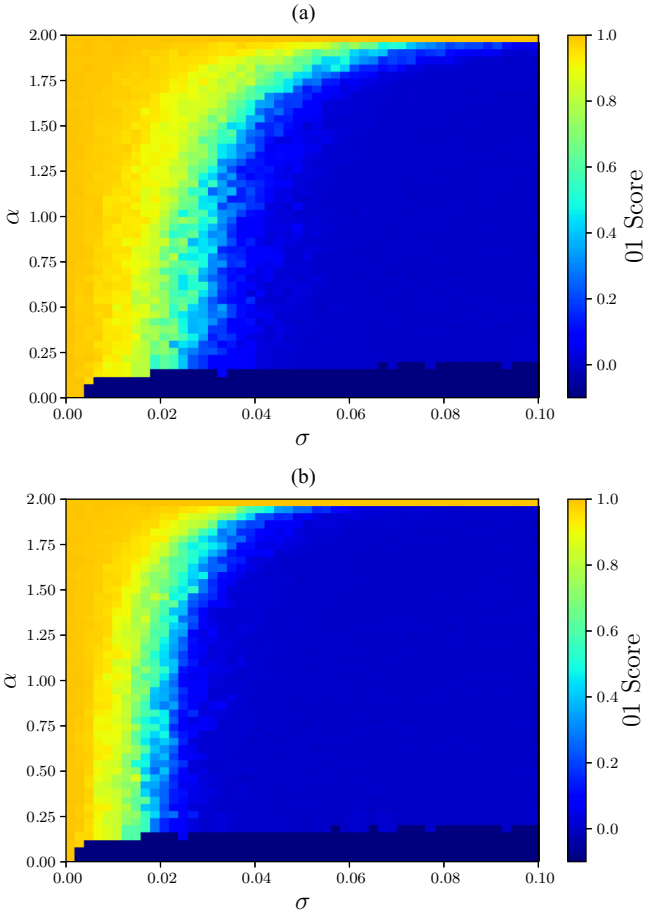

FIG. 8. Heat maps of the objective score function for $U^{(01)}(\alpha, \sigma)$ in the stable Lévy noise case with $\phi = 0.96\pi$, $\psi = 0$, and 100 iterations for $T = 6000$; (a) is the one-sided and (b) is the two-sided case. High scoring (dark yellow) values correspond to O_R steady or periodic behavior, low scoring nonzero values (light blue) correspond to noise, and negative values (dark blue) correspond to long transients in the times series.

two examples of computation of $U^{(01)}$ for stable ($\lambda = 0$) and tempered stable (varying across λ), in Figs. 8 and 9, where yellow indicates ordered regions and blue noisy regions. We choose a case of $\phi = 0.96\pi$, $\psi = 0$ where $\mathcal{K} > 0$ and therefore we know that the deterministic dynamics should be constant in quantities such as O_B, O_R, and Δ.

For the stable case, we show both one-sided (top panel) and two-sided (bottom panel) cases in Fig. 8. We observe that across all values of α, for $\sigma > 0.05$ there is an onset of noise with the strongest departures to noise at low α consistent with the property that tails in the noise distribution become very heavy. Evidently, the role of skew in the noise plays a marginal role.

Contrastingly, we now choose $\sigma = 0.05$ and explore the tempered stable case in Fig. 9 for $\phi = 0.96\pi$ for both the one-sided ($\theta = 1$) (top) and symmetric ($\theta = 0$) (bottom) cases. We see that close to the Gaussian regime $\alpha \approx 2$, there is an absence of noisy behavior across all values of λ, as to be expected. We also see that for $\lambda = 0$, going vertically down the left hand edge of the plot, there is a transition from steady to periodic behavior, to noisy behavior, and then long

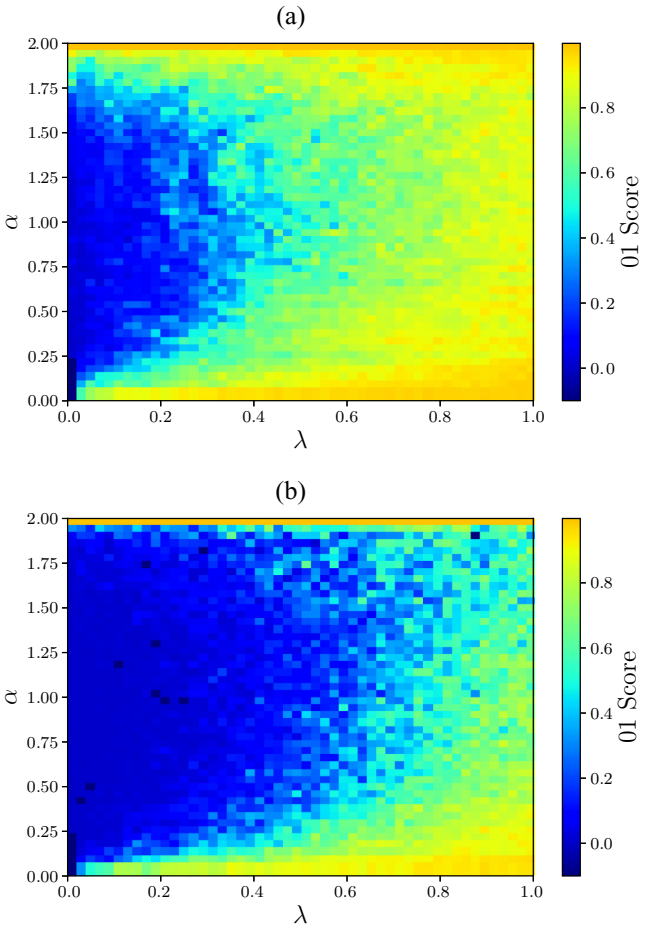

FIG. 9. Heat maps of the objective score function for $U^{(01)}(\alpha, \lambda)$ in the tempered stable Lévy noise case, with $\psi = 0$, $\sigma = 0.05$, and 100 iterations for $T = 6000$; top for the one-sided $\phi = 0.96\pi$ and bottom for the two-sided case with $\phi = 0.96\pi$. High scoring (dark yellow) values correspond to O_R steady or periodic behavior, low scoring nonzero values (light blue) correspond to noise, and negative values (dark blue) correspond to long transients in the times series.

transients, reflecting the structure of the landscape for the stable case in Fig. 8. However, once $\lambda \neq 0$ this monotonic trend from steady state to noisy behavior changes. For any fixed $0 < \lambda < 0.3$ as α decreases there is a transition to noisy behavior and then back to periodic behavior (yellow goes to blue which goes back to yellow). Thus, there is a *restoration* of ordered behavior for all λ for *small* values of α, typically $\alpha \leqslant 0.25$.

In other words, blue and red will exhibit smoother periodic behavior in relation to each other. This is broadly consistent with the pattern observed analytically for the dynamics of Δ using the ratchet potential in the zero mode projection of the blue-vs-red system. Recall three significant effects were seen to occur in that approach: the skew drops out, there is a greater suppression of variance in Δ for small α for nonzero λ, and there is a reduction of the average drift between blue and red clusters. That the skew does not play a role can be seen in the result for the landscape of for $U^{(01)}$ for zero skew (namely, symmetric two-sided noise) in the bottom panel, with $\phi = 0.96\pi$ again. Once more, we observe the suppression of noisy behavior at small α. Although the onset of noisy behavior is more general in the full system, applying between and within blue and red. However, the analytical result for the variance of Δ and the average value of $\dot{\Delta}$ shows that the generation, or suppression, of variability in the zero mode of the system is *consistent* with this behavior. Of course, there is need for caution, as the analytic approach is not valid in the deep noisy regime; the *onset* of drift and variation from the noise is a precursor to the stronger regime of noisy behavior. In this sense, we may say there is qualitative agreement between numerical and analytical results on the impact of small α in suppressing the tendency to noisy behavior of the nearly locked blue-red system in the presence of tempering; increasing the exponent of the tail of the distribution does not disrupt blue and red locking with monotonically increasing strength. The observation of this, and the broad consistency between analytical and numerical approaches, are the main results of this paper.

TABLE I. Bayesian optimization results for $U(\psi, \phi, \xi_{BR}, \xi_{RB})$ where $\psi, \phi \in [0, 2\pi]$ and $\xi_{BR}, \xi_{RB} \in (0, 1]$ for 500 iterations and $T = 2000$. $\sigma = 0.05$, $\alpha = 1.5$, and $\lambda = 0.75$.

		Parameters			
Noise	U	ψ	ϕ	ζ_{BR}	ζ_{RB}
None	57.8598	1.675π	0.1944π	0.8997	0.1628
Gaussian	98.6311	1.3747π	0.0033π	0.8170	0.0668
Stable	10.6854	0.2007π	0.0083π	0.8289	0.7124
T. Stable	42.0838	1.2693π	0.0143π	0.9932	0.1017

H. Optimization across multiple parameters

We have seen throughout the work that the nonlinear nature of the interactions in the blue-vs-red model means that, even deterministically, it is not generally possible for one population, say blue, to achieve the desired phase ahead of the other, for example ϕ. We now use the Bayesian approach to search for optima *for blue* across the four cross-population parameters $\phi, \psi, \zeta_{BR}, \zeta_{RB}$ given the blue and red networks and internal couplings ζ_B, ζ_R as previously given. We conduct 500 iterations running the simulation out to $T = 2000$ and consider four cases: deterministic, Gaussian (as used in [8]), stable ($\alpha = 1.5$), and tempered stable ($\alpha = 1.5, \lambda = 0.75$). The results are shown in Table I.

We note that the Gaussian case obtained a higher scoring optimal value than the deterministic case as a result of either a relativity small number of optimization iterations for a four-dimensional parameter space and the algorithm favoring a local maximum. The optimization algorithm was unable to find a decently scoring set of parameters in the stable Lévy noise case. We observe nevertheless a broad consistency between the three other cases in that $\psi > \phi$ and $\zeta_{BR} > \zeta_{RB}$. In the interests of space, we forego here showing plots of the corresponding time series for $O_{B,R}$ and $\Delta(t)$ but simply comment that O_B shows generally higher values than O_R, and $\Delta(t)$ is a positive constant for deterministic ($\Delta \approx 0.6$) and Gaussian ($\Delta \approx 0.01$) cases. For the tempered stable case, the expected value of Δ is approximately 0.06, however, the extreme cases are time varying both positively and negatively, not untypical for $1 < \alpha < 2$. The requirement that Δ is close

to ϕ is part of the objective function U_2 ensures that blue comes as close as possible to its objective by not seeking to be as ambitious in its phase ahead of red as red seeks in its relation to blue. The actual values of Δ match ϕ for the deterministic and Gaussian cases. On the other hand, to achieve this, blue agents must seek to couple to red agents more strongly than red to blue; the nature of the internal networks intuitively plays an important role in this, just as blue's hierarchy requires stronger internal coupling to achieve its level of internal synchronization. Stable noise is generally destructive of such optima outside the narrow range where one population complies with the intent of the other (for example, $\phi = -\psi$), as previous results have emphasized. These results are simply a taste of what is possible with such a model. Future work may consider optimization across more parameters and ultimately across different networks.

VI. CONCLUSIONS

We have explored the two networked populations "blue-vs-red" frustrated Kuramoto model subject to tempered stable noise. Using approximations in the region where the two populations are internally synchronized but seek to lock with respect to each other, we have solved the stochastic dynamics using the tempered fractional Fokker-Planck approach. The zero-mode projection under the graph Laplacian of this reveals that, whereas for $1 < \alpha < 2$, noise generally causes an otherwise deterministically locked system to degrade, leading to drift between blue and red clusters, for small $\alpha < 1$ improved locking between blue and red takes place. In the situation where deterministically the system shows locking, the noise may be such that stochastically induced drift between blue and red is entirely canceled. When the deterministic system exhibits drift between blue and red clusters, such tempered stable noise can be used to moderate the stochastic drift.

Through our simulations we see a similar pattern: noise of higher strength or stronger tails can disrupt the locking between blue and red in cases where deterministically the system may be achieving high levels of global synchronization, with both sets of agents well synchronized internally and having a fixed frustration in relation to each other. Tempering, naturally, has the effect of restoring locking by moderating the heavy tails. The surprising result we find is that with tempering in the regime where $\alpha < 1$ the system may become less noisy, and thus showing smoother periodic, and approaching steady state, behavior. Again, this is consistent with blue and red either smoothly drifting in relation to each other or even locking. There is only the caveat that the analytical result does not apply in the noisy regime, but provides an indicator or precursor to it.

Thus, both analytically and numerically we obtain a surprising result, that the boundaries of regions of different dynamics (steady state, periodic, noisy behavior) of the stochastic system are not linear in variation of the parameter α governing the tail of the noise once tempering is introduced. In contrast, for purely stable noise reducing α only destroys locking between blue and red with monotonically increasing severity.

Intuitively, we propose that the underlying reason for this behavior lies in an interplay of the ratchet mechanism with tempering and the fundamental change in the stable noise probability density for $\alpha < 1$. As illustrated in [28], for $\alpha < 1$ the density is no longer centered around zero but with a heavy tail that is increasingly suppressed as λ increases. This centering becomes the dominant effect with tempering, and seemingly acts to counter the deterministic drift in the ratchet potential.

Importantly, much of the structure of the landscape of the stochastic system, as determined through simulation, can be predicted through the analytically accessible thresholds for instability and periodic behavior from the deterministic system at least with weak noise strength. Thus, analytic understanding of the landscape in the absence of noise remains an important guide to the overall structure of the landscape of dynamics in the regime of weak noise, close to the boundary with noisy behavior. These insights are then complemented by examining the Laplacian zero mode projection of the linearized system, where the properties of ratchet potentials under tempered stable noise play an important, and analytically tractable, role in predicting the weak noise strength dynamics. This nonlinear mechanism, with tilted ratchet potentials, has not been articulated before in the context of synchronization on multinetworks.

Interpreting these results in the context of the competitive system of blue and red agents is now interesting. Intuitively, it is clear that if two populations both seek to maintain a certain phase advantage over the other, it is not possible for both to simultaneously achieve their aims. For different network structures and couplings, one side or the other may be able to achieve close to their result within a certain bound. Indeed, our results show that in such interactions "less is more," namely, that one side seeking less ambitious phase advantage in relation to the other may be able to achieve more optimal results. The landscape method shown here enables determination of these boundaries before instability is triggered, and how close to optimality may be achieved. The added dimension of noise, in general, makes this optimal behavior even more difficult. However, for certain forms of non-Gaussian noise with tempering λ for large jumps and far-from-Gaussian power law index α better approach to optimal behavior may be achieved. Indeed, such behavior becomes attractive as a mechanism for guiding the behavior of otherwise complex competitive stochastic systems or informing an understanding of the capacity for resilience or robustness of the system. As alluded already, future work may broaden the scope of the optimization to cover the networks themselves. For example, for a given topology, or statistical parametrization thereof, of red what is the optimal network within and across for blue? Returning to our overall aim to apply such models to competitive distributed decision making or social processes, investigations like this with the two-network frustrated Kuramoto model open the door for testing many rather qualitative hypotheses in the organizational, social, and management science literature.

ACKNOWLEDGMENTS

A.C.K. is supported through a Chief Defence Scientist Fellowship and is grateful for ANU hospitality. This research

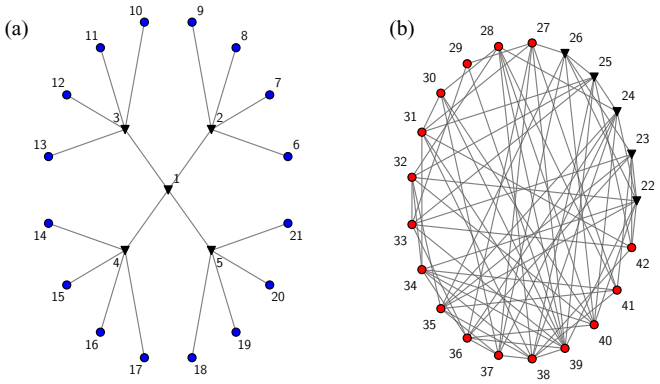

FIG. 10. (a) The blue network and (b) the red network used in the numerical simulation of Eq. (1) with noise.

was a collaboration between the Commonwealth of Australia (represented by the Defence Science and Technology Group) and the Australian National University through a Defence Science Partnerships agreement.

APPENDIX A: DEFINITIONS FOR THE LINEARIZED BLUE-VS-RED MODEL

We define the quantities d and L used in the main body, drawing basic concepts from graph theory [38]. The *degree* of blue agent at node $i \in \mathscr{B}$ is the number of links from node i to other blue agents,

$$d_i^{(B)} \equiv \sum_{j\in\mathscr{B}} \mathscr{B}_{ij}, \quad i \in \mathscr{B}.$$

The corresponding blue *degree matrix* $\mathscr{D}^{(B)}$ is a diagonal matrix with the degrees $d_i^{(B)}$ inhabiting the diagonal entries

$$\mathscr{D}_{ij}^{(B)} \equiv d_i^{(B)}\delta_{ij}, \quad \{i,j\} \in \mathscr{B}.$$

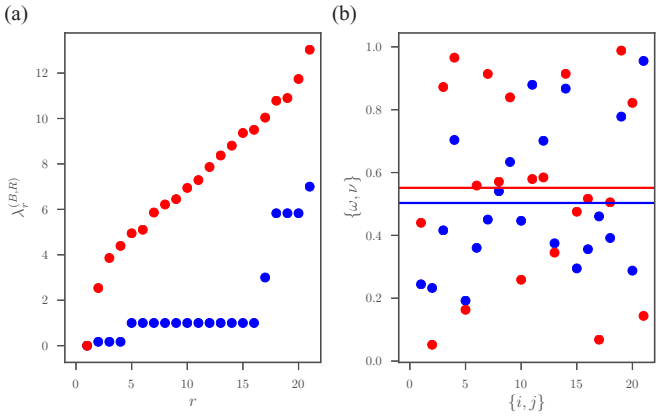

FIG. 11. (a) The spectrum of the graph Laplacian for blue and red networks colored, respectively, blue and red. (b) The frequencies for blue and red agents according to the node labeling again colored blue and red, respectively, with solid lines indicating their corresponding means.

The matrices L in Eq. (17) constitute a *graph Laplacian*, where the Laplacian for the blue population is given by the expression

$$L_{ij}^{(B)} \equiv \mathscr{D}_{ij}^{(B)} - \mathscr{B}_{ij}, \quad \{i,j\} \in \mathscr{B}.$$

Equivalent definitions for $L^{(R)}$ apply to the red network.

Addressing the corresponding cross-network quantities, we define the degree with which a blue agent at node i connects to red agents as

$$d_i^{(BR)} \equiv \sum_{j\in\mathscr{B}\cup\mathscr{R}} \mathscr{M}_{ij} = \sum_{j\in\mathscr{R}} \mathscr{A}_{ij}^{(BR)}, \quad i \in \mathscr{B}.$$

We note that in this instantiation of the model $\mathscr{A}^{(BR)}$ is the transpose of $\mathscr{A}^{(RB)}$, and vice versa (it need not be so, however), so there is symmetry between the total number of degrees between the blue and red networks:

$$d_T^{(BR)} = d_T^{(RB)} = \sum_{i\in\mathscr{B}} d_i^{(BR)} = \sum_{i\in\mathscr{R}} d_i^{(RB)}. \tag{A1}$$

The diagonal degree matrix $\mathscr{D}^{(BR)}$ which encodes all the blue to red links is given by

$$\mathscr{D}_{ij}^{(BR)} \equiv d_i^{(BR)}\delta_{ij}, \quad i \in \mathscr{B}, \quad j \in \mathscr{B}\cup\mathscr{R},$$

where the final M diagonal entries of $\mathscr{D}^{(BR)}$ are zero. This finally leads to the cross-network Laplacian from blue to red:

$$L_{ij}^{(BR)} \equiv \mathscr{D}_{ij}^{(BR)} - \mathscr{M}_{ij}, \quad i \in \mathscr{B}, \quad j \in \mathscr{B}\cup\mathscr{R}.$$

Similar considerations lead to an equivalent expression for the red to blue cross-network Laplacian $L^{(RB)}$.

The blue and red network Laplacians obey the following eigenvalue equations:

$$\sum_{j\in\mathscr{B}} L_{ij}^{(B)} e_j^{(B,r)} = \lambda_r^{(B)} e_i^{(B,r)}, \quad i \in \mathscr{B}$$

$$\sum_{j\in\mathscr{R}} L_{ij}^{(R)} e_j^{(R,r)} = \lambda_r^{(R)} e^{(R,r)}{}_{,i} \quad i \in \mathscr{R}.$$

The graph eigenvalues are well-studied objects [38]. For instance, the *zeroth* eigenvalue is always zero valued, and the remaining eigenvalues are all real, positive, semidefinite, and can be ordered as follows:

$$0 = \lambda_0^{(B)} \leqslant \lambda_1^{(B)} \leqslant \lambda_2^{(B)} \leqslant \cdots \leqslant \lambda_N^{(B)},$$

where we have used the blue network as an example. The normalized zero eigenvectors are

$$e_i^{(B,0)} = \frac{1}{\sqrt{N}} \quad i \in \mathscr{B}, \qquad e_i^{(R,0)} = \frac{1}{\sqrt{M}} \quad i \in \mathscr{R}.$$

They provide an alternate expression for the blue and red centroids:

$$B = \frac{1}{\sqrt{N}} \sum_{i\in\mathscr{B}} \beta_i e_i^{(B,0)}, \qquad P = \frac{1}{\sqrt{M}} \sum_{j\in\mathscr{R}} \rho_j e_j^{(R,0)}.$$

Projections onto the eigenvectors are

$$\omega^{(s)} = \sum_{i\in\mathscr{B}} \omega_i e_i^{(B,s)}, \quad \bar{\omega} = \frac{1}{N}\sum_{i\in\mathscr{B}} \omega_i,$$
$$d_s^{(BR)} = \sum_{i\in\mathscr{B}} d_i^{(BR)} e_i^{(B,s)},$$

and equivalent expressions hold for the relevant red quantities.

Fluctuations b_i and p_j are expanded in the following nonzero *normal modes*:

$$b_i = \sum_{r\in\mathscr{B}^E/\{0\}} x_r e^{(B,r)}{}_{,i} \quad i \in \mathscr{B},$$
$$p_j = \sum_{r\in\mathscr{R}^E/\{0\}} y_r e_j^{(R,r)}, \quad j \in \mathscr{R}. \tag{A2}$$

APPENDIX B: NETWORKS AND FREQUENCIES USED IN NUMERICAL CALCULATIONS

As mentioned in the main body, a tree network was used for blue and a random graph for red. Blue-to-red interactions are arranged such that each leaf node of blue ($i = 6, \ldots, 21$) interacts with the correspondingly labeled red node ($i = 27, \ldots, 42$), shown as open circles in Fig. 10. Thus, $d_i^{(BR)} = d_i^{(RB)} = 1$ or 0, for agents engaged, respectively not engaged, with a competitor, but $d_T^{(BR)} = 16$. Given the significance of the graph Laplacians we show their spectra and the frequencies of each agent in Fig. 11. Note here that there are many more low lying eigenvalues for $L^{(B)}$ compared to $L^{(R)}$, a consequence of the comparatively poor connectivity of the tree graph [Fig. 11(a)].

[1] Y. Kuramoto, *Chemical Oscillations, Waves and Turbulence* (Springer, Berlin, 1984).

[2] S. H. Strogatz, From Kuramoto to Crawford: exploring the onset of synchronization in populations of coupled oscillators, Phys. D (Amsterdam) **143**, 1 (2000).

[3] J. A. Acebrón, L. Bonilla, C. Pérez Vincente, F. Ritort, and R. Spigler, The Kuramoto model: A simple paradigm for synchronization phenomena, Rev. Mod. Phys. **77**, 137 (2005).

[4] S. N. Dorogovtsev, A. V. Goltsev, and J. F. F. Mendes, Critical phenomena in complex networks, Rev. Mod. Phys. **80**, 1275 (2008).

[5] A. Arenas, A. Díaz-Guilera, J. Kurths, Y. Moreno, and C. Zhou, Synchronization in complex networks, Phys. Rep. **469**, 93 (2008).

[6] F. Dörfler and F. Bullo, Synchronization in complex networks of phase oscillators: A survey, Automatica **50**, 1539 (2014).

[7] A. C. Kalloniatis and M. Zuparic, Fixed points and stability in the two-network frustrated Kuramoto model, Phys. A (Amsterdam) **447**, 21 (2016).

[8] A. B. Holder, M. L. Zuparic, and A. C. Kalloniatis, Gaussian noise and the two-network frustrated Kuramoto model, Phys. D (Amsterdam) **341**, 10 (2017).

[9] H. Sakaguchi and Y. Kuramoto, A soluble active rotator model showing phase transitions via mutual entertainment, Prog. Theor. Phys. **76**, 576 (1986).

[10] A. C. C. Coolen and C. Pérez-Vicente, Partially and frustrated coupled oscillators with random pinning fields, J. Phys. A: Math. Gen **36**, 4477 (2003).

[11] V. Nicosia, M. Valencia, M. Chavez, A. Díaz-Guilera, and V. Latora, Remote Synchronization Reveals Network Symmetries and Functional Modules, Phys. Rev. Lett. **110**, 174102 (2013).

[12] S. Kirkland and S. Severini, α-Kuramoto partitions from the frustrated Kuramoto model generalise equitable partitions, Applicable Anal. Discrete Math. **9**, 29 (2015).

[13] A. Kalloniatis, From incoherence to synchronicity in the network Kuramoto model, Phys. Rev. E **82**, 066202 (2010).

[14] S. Boccaletti, G. Bianconi, R. Criado, C. I. del Genio, J. Gómez-Gardeñes, M. Romance, I. Sendiña-Nadal, Z. Wang, and M. Zanin, The structure and dynamics of multilayer networks, Phys. Rep. **544**, 1 (2014).

[15] E. Montbrió, J. Kurths, and B. Blasius, Synchronization of two interacting populations of oscillators, Phys. Rev. E **70**, 056125 (2004).

[16] E. Barreto, B. Hunt, E. Ott, and P. So, Synchronization in networks of networks: The onset of coherent collective behavior in systems of interacting populations of heterogeneous oscillators, Phys. Rev. E **77**, 036107 (2008).

[17] Y. Kawamura, H. Nakao, K. Arai, H. Kori, and Y. Kuramoto, Phase synchronization between collective rhythms of globally coupled oscillator groups: Noiseless identical case, Chaos **20**, 043110 (2010).

[18] P. S. Skardal and J. G. Restrepo, Synchronization of Kuramoto oscillators in networks of networks, *2012 International Symposium on Nonlinear Theory and its Applications NOLTA2012*, Palma, Majorca, Spain, October 22–26, 2012, pp. 171–174, arXiv:1206.3822v1.

[19] B. C. Bag, K. G. Petrosyan, and C. K. Hu, Influence of noise on the synchronization of the stochastic Kuramoto model, Phys. Rev. E **76**, 056210 (2007).

[20] H. Khoshbakht, F. Shahbazi, and K. A. Samani, Phase synchronization on scale-free and random networks in the presence of noise, J. Stat. Mech.: Theory Exp. (2008) P10020.

[21] R. Tönjes, Synchronization transition in the Kuramoto model with colored noise, Phys. Rev. E **81**, 055201(R) (2010).

[22] M. L. Zuparic and A. C. Kalloniatis, Stochastic (in)stability of synchronisation of oscillators on networks, Phys. D (Amsterdam) **255**, 35 (2013).

[23] R. K. Esfahani, F. Shahbazi, and K. A. Samani, Noise-induced synchronization in small world networks of phase oscillators, Phys. Rev. E **86**, 036204 (2012).

[24] L. DeVille, Transitions amongst synchronous solutions in the stochastic Kuramoto model, Nonlinearity **25**, 1473 (2012).

[25] D. Traxl, N. Boers, and J. Kurths, General scaling of maximum degree of synchronization in noisy complex networks, New J. Phys. **16**, 115009 (2014).

[26] Y. Kawamura, H. Nakao, K. Arai, H. Kori, and Y. Kuramoto, Phase synchronization between collective rhythms of globally coupled oscillator groups: Noisy identical case, Chaos **20**, 043109 (2010).

[27] A. C. Kalloniatis and D. O. Roberts, Synchronisation of networked Kuramoto oscillators under stable Lévy noise, Phys. A (Amsterdam) **466**, 476 (2017).

[28] D. O. Roberts and A. C. Kalloniatis, Synchronisation under shocks: the Lévy Kuramoto model, Phys. D (Amsterdam) **368**, 10 (2018).

[29] R. Metzler and J. Klafter, The random walker's guide to anomalous diffusion: A fractional dynamics approach, Phys. Rep. **339**, 1 (2000).

[30] R. Metzler and J. Klafter, The restaurant at the end of the random walk: Recent developments in the description of anomalous transport by fractional dynamics, J. Phys. A: Math. Gen. **37**, R161 (2004).

[31] R. N. Mantegna and H. E. Stanley, Stochastic Process with Ultraslow Convergence to a Gaussian: The Truncated Lévy Flight, Phys. Rev. Lett. **73**, 2946 (1994).

[32] I. Koponen, Analytic approach to the problem of convergence of truncated Lévy flights towards the Gaussian stochastic process, Phys. Rev. E **52**, 1197 (1995).

[33] A. Kullberg and D. del-Castillo-Negrete, Transport in the spatially tempered, fractional Fokker-Planck equation, J. Phys. A: Math. Theor. **45**, 255101 (2012).

[34] D. del-Castillo-Negrete, Anomalous transport in the presence of truncated Lévy flights, in *Fractional Dynamics: Recent Advances*, edited by J. Klafter, S. Lim, and R. Metzler (World Scientific, Singapore, 2012), p. 129–57.

[35] K. I. Sato, *Lévy Processes and Infinitely Divisible Distributions* (Cambridge University Press, Cambridge, 1999).

[36] I. Podlubny, *Fractional Differential Equations* (Academic, San Diego, 1999).

[37] S. Samko, A. Kilbas, and O. Marichev, *Fractional Integrals and Derivatives: Theory and Applications* (CRC Press, London, 1993).

[38] B. Bollobás, *Modern Graph Theory*, Graduate Texts in Mathematics (Springer, New York, 1998).

[39] L. M. Pecora and T. L. Carroll, Master Stability Functions for Synchronized Coupled Systems, Phys. Rev. Lett. **80**, 2109 (1998).

[40] B. Linder, M. Kostur, and L. Schimansky-Geier, Optimal diffusive transport in a tilted periodic potential, Fluctuat. Noise Lett. **1**, R25 (2001).

[41] A. K. Lee, J. R. Lee, and K. H. Lee, Asymmetric step-like characteristics in a tilted rocking ratchet potential, Phys. B (Amsterdam) **407**, 4298 (2012).

[42] K. J. Challis and M. W. Jack, A tight-binding approach to overdamped brownian motion on a multidimensional tilted periodic potential, Phys. Rev. E **87**, 052102 (2013).

[43] P. Reimann, Brownian motors: Noisy transport far from equilibrium, Phys. Rep. **361**, 57 (2002).

[44] M. L. Zuparic and A. C. Kalloniatis, Analytic solution to fractional Fokker-Planck equations for tempered-stable Lévy distributions with spatially linear, J. Phys. A: Math. Theor. **51**, 035101 (2018).

[45] A. Cartea and D. del-Castillo-Negrete, Fluid limit of the continuous-time random walk with general Lévy jump distribution functions, Phys. Rev. E **76**, 041105 (2007).

[46] A. Polyanin, *Handbook of Linear Partial Differential Equations for Engineers and Scientists* (Chapman Hall/CRC, Boca Raton, FL, 2002).

[47] M. L. Zuparic, A. C. Kalloniatis, and D. O. Roberts, Noise-driven current reversal and stabilisation in the tilted ratchet potential subject to tempered stable Lévy noise, Phys. Rev. E **96**, 052116 (2017).

[48] B. D. McKay, Practical graph isomorphism, Congr. Numer. **30**, 45 (1981).

[49] C. E Rasmussen and C. K. I. William, *Gaussian Processes for Machine Learning* (MIT Press, Cambridge, MA, 2006), Vol. 1.

[50] J. Snoek, H. Larochelle, and R. P. Adams, Practical Bayesian optimization of machine learning algorithms, in *Advances in neural information processing systems 25*, edited by F. Pereira, C. J. C. Burges, L. Bottou, and K. Q. Weinberger (Curran Associates, Inc., Red Hook, NY, 2012), pp. 2951–2959.

[51] F. Nogueira, BAYESIANOPTIMIZATION: A Python implementation of global optimization with Gaussian processes, github.com/fmfn/BayesianOptimization

[52] G. A. Gottwald and I. Melbourne, A new test for chaos in deterministic systems, Proc. R. Soc. London A **460**, 603 (2004).

[53] G. A. Gottwald and I. Melbourne, On the implementation of the 0-1 test for chaos, SIAM J. Appl. Dyn. Syst. **8**, 129 (2009).